

# **Investigation of Thin Film Supercurrent and Photodetection in Wide Niobium Nitride Wires**

by

Owen Medeiros

B.S., Wentworth Institute of Technology (2019)

Submitted to the Department of Electrical Engineering and Computer Science  
in partial fulfillment of the requirements for the degree of

Master of Science

at the

MASSACHUSETTS INSTITUTE OF TECHNOLOGY

May 2022

© Massachusetts Institute of Technology 2022. All rights reserved.

Author .....  
Department of Electrical Engineering and Computer Science  
May 13, 2022

Certified by .....  
Karl K. Berggren  
Professor of Electrical Engineering and Computer Science  
Thesis Supervisor

Accepted by .....  
Leslie A. Kolodziejski  
Professor of Electrical Engineering and Computer Science  
Chair, Department Committee on Graduate Students



# **Investigation of Thin Film Supercurrent and Photodetection in Wide Niobium Nitride Wires**

by

Owen Medeiros

Submitted to the Department of Electrical Engineering and Computer Science  
on May 13, 2022, in partial fulfillment of the  
requirements for the degree of  
Master of Science

## **Abstract**

Over the past two decades, superconducting nanowire single photon detectors have become the dominant platform for detection at telecommunication wavelengths. Despite their practical success, the theoretical framework that describes the detection mechanism within the nanowire is continually evolving. Early phenomenological models suggested that a hot region forms across the superconducting strip after the arrival of a photon, producing a measurable voltage only if the diameter of the hot region extends across the width of the strip. However, predictions based on the kinetic-equation approach showed that within a certain operating regime detection no longer depends on the strip's width. This prediction was later supported by the experimental demonstration of single photon detection in strips 1-3  $\mu\text{m}$  wide. The ability to fabricate detectors with larger widths would allow for higher signal to noise ratios as well as higher fabrication yield compared to narrow wires. These advantages could potentially unlock some long sought after applications of single photon detectors such as large area detectors or >kilopixel arrays of detectors. In order to produce wide wire detectors the design and material properties must be well optimized. This thesis will cover the development of wide single photon detectors using nitrogen rich niobium nitride.

Thesis Supervisor: Karl K. Berggren  
Title: Professor of Electrical Engineering and Computer Science



*To my parents.*



## Acknowledgments

This work would not have been possible without the support of my family, friends and colleagues, and I would like to take this opportunity to thank a few of them here.

To my advisor Karl Berggren for his guidance and dedication, and for creating an environment that promotes scientific growth. Without his direction, I would have been unable to experience the joy of scientific discovery.

To my mentor Marco Colangelo, who has helped me through every aspect of my graduate studies, and life, over the past few years. I am continually impressed by his drive and continually surprised by his humor.

To Brenden Butters, for his limitless expertise and patience, and for instilling confidence in my abilities.

To Navid Abedzadeh, Andrew Dane, Murat Onen, John Simonaitis, Emily Toomey, and Marco Turchetti for welcoming me to MIT and making work a jovial place.

To Matteo Castellani, for his passion and excitement for superconducting circuits. I could not hope for a better colleague and I am eager to see what we can accomplish.

To Jim Daley and Mark Mondol for their support for all things related to nanofabrication, and to Charlie Settens for his support in x-ray crystallography.

To the members of the QNN group, for their research advice, camaraderie, and the daily discussions by the coffee machine.

To Donnie Keathley, Yugu Yang-Keathley, and Joseph Martel-Foley, for guiding my first steps into research. Their commitment to expanding access to higher education has enabled the opportunities I have today.

To my friends, for reminding me how to have fun, and for making all other aspects of my life wonderful.

To my grandparents, for all the love they have showed me and for keeping me well fed.

To my sister, for being the person I can turn to when things are at their worst, and for reminding me that the best things are yet to come.

Most of all to my parents, without them I would not be the person I am today. They have been incredible role models and I am overwhelmingly grateful for the values they have instilled.



# Contents

<b>1</b>	<b>Introduction</b>	<b>21</b>
1.1	Theoretical description of thin film supercurrent . . . . .	21
1.1.1	Macroscopic theory . . . . .	22
1.1.2	Microscopic theory . . . . .	26
1.2	Micrometer wide superconducting single photon detectors . . . . .	28
1.2.1	Detection in micrometer wide wires . . . . .	28
1.2.2	Experimental evidence . . . . .	30
<b>2</b>	<b>Current Distribution and Reproducibility in Wide Strips</b>	<b>33</b>
2.1	Quasiclassical description . . . . .	33
2.2	Experimental setup . . . . .	35
2.2.1	Fabrication . . . . .	36
2.2.2	Measurement . . . . .	37
2.3	Critical current measurements . . . . .	39
2.3.1	Length . . . . .	40
2.3.2	Width . . . . .	42
<b>3</b>	<b>Nitrogen Rich Niobium Nitride</b>	<b>49</b>
3.1	Introduction . . . . .	49
3.2	Electrical and optical characterization . . . . .	51
3.3	Atomic structure characterization . . . . .	54
3.3.1	X-Ray diffraction . . . . .	55
3.3.2	Transmission electron microscopy . . . . .	56

<b>4 Micrometer Wide Single Photon Detectors</b>	<b>61</b>
4.1 Design and fabrication of wide detectors . . . . .	62
4.1.1 Design . . . . .	62
4.1.2 Fabrication . . . . .	63
4.2 Cryogenic measurement and data processing . . . . .	64
4.2.1 Cryogenic setup . . . . .	65
4.2.2 SNSPD measurement . . . . .	66
4.3 Detector performance . . . . .	70
4.3.1 Material comparison . . . . .	70
4.3.2 Wide detector performance . . . . .	71
4.3.3 Conclusion . . . . .	75
<b>A Supporting information</b>	<b>77</b>

# List of Figures

1-1 Numerical simulation of the vector potential in a two-dimensional superconducting strip. Left, a superconducting strip where the vector potential in the strip is equal to Eq. 1.8, and zero outside. Dirichlet boundary conditions define  $A = 1$  at the horizontal boundaries, corresponding to maximum current on the edges. For each width, a cut line (dashed line) was integrated to determine the amount of screening  $1 - \int J_c(x)/w$ . Right, the screening as a function of width. For the smallest widths the current distribution is near uniform and screening is zero. As the width increases the current is screened from the center. The inset plots Eq. 1.16 for the bulk and thin film case. . . . . 24

2-1 (a) The nonlinear, nonmonotonic material relation. Note this function is assumed to be constant in the London model. (b) Current screening in a superconducting strip. The dashed lines represent the screening determined by the London model. The solid lines represent the screening determined by the quasiclassical model. For each penetration depth shown the London model underestimates the amount of current in the strip. (c) The temperature dependent coefficients  $c(T)$  and  $\kappa(T)$ . Figures reproduced from [47]. . . . . 35

2-2 Typical setup for critical current measurements in liquid helium. Right, the rf probe immersed in liquid helium. Center, a schematic of the room temperature electronics and sample mounting. Left, the instruments used and a typical waveform of a nanowire biased beyond  $I_c$  with a triangular wave. . . . . 39

- 2-3 Scanning electron micrograph of two wires with test points spaced 200  $\mu\text{m}$  apart. The dark regions indicate the NbN film and the light gray regions indicate the substrate. . . . . 40
- 2-4 Critical current measurements at different test points. The filled box plot corresponds to measurements of increasing length, measured from the test point to zero. The empty box plots correspond to fixed-length measurements between adjacent test points. The empty boxes are less suppressed by cumulative constrictions along the wire. . . . . 41
- 2-5 Left, average critical current of each wire at three temperatures. The solid lines predict  $I_c(w, T)$  with  $\lambda$  following the two fluid temperature approximation calculated from the fitting of the 4.2 K data,  $\lambda_{4.2}(0)$ . The dashed lines fit  $\lambda$  at each temperature, thus the solid and dashed curves for 4.2 K are identical. The inset shows the linear region  $w \ll \Lambda_p(T)$  with the same units as main axes. Right, The temperature dependence of  $\lambda_{4.2}(T)$  is plotted over the fraction of the critical temperature. The circles represent the penetration depth determined from the direct fitting (dashed lines in the left figure). The circles do not agree with the expected behavior  $\lambda_{4.2}(T)$ . To correctly predict the temperature dependence of the penetration depth a reduction in the critical temperature  $T_c^*$  is needed. . . . . 43
- 2-6 Left, temperature dependent critical current density for various widths. The black line was calculated from the highest critical current measurement  $J_c^{0.3}$ . Right, the same data normalized by  $J_c^{0.3}$ . The 0.3  $\mu\text{m}$  wire is the least constricted while most narrow wires are clustered at  $0.8 J_c^{0.3}$ . As the width increases we see the current density is reduced. As the temperature increases  $J_c$  becomes less suppressed, and the gain is proportional to the width. Near 8.5 K,  $J_c$  starts to decrease, returning closer to the expected temperature dependence. . . . . 44
- 2-7 Interpolated data from the measured data in Figure 2-6. The change in the critical current density relative to the expected temperature dependence as a function of width and temperature. This used as a correction factor to the quasiclassical model. 45

- 2-8 The predicted  $I_c$  from the quasiclassical model with the  $J_c$  correction coefficient. This figure is identical to Figure 2-5 but with the correction shown in Figure 2-7. Left, the solid lines show the expected temperature dependence calculated from the 4.2 K data. The dashed lines represent the fit of the quasiclassical model with the correction coefficient. The correction coefficient is depicted as that shaded region between the dashed and solid lines. Right, the penetration depth determined from the quasiclassical model. With the correction,  $\lambda(T)$  now aligns with the expected trend. . . . . 46
- 2-9 Predicted critical current using the interpolated temperature sweep data. Left, the solid lines show the expected BCS temperature dependence. The dashed lines show the fitted temperature dependence with the correction coefficient (shaded region). Right, the penetration depth of the interpolated data without the correction (circles), and the corresponding effective critical temperature  $T_c^*$ , and the penetration depth with the correction (dots),  $T'_c$ . The solid line shows the expected temperature dependence. . . . . 47
- 2-10 A cross section of a thin superconducting strip wider than the Pearl length. The solid blue line, maximum at NS boundary, combines the suppression in the center of a wire due to the Pearl length screening and the decay to the edges due to the proximity effect. Its integral, shaded in blue, is greater than the distribution of current extending over the entire width, shaded in green. The red dashed line represents the proximity effect in a wire modeled as a normal-superconducting-normal (NSN) lateral stack. A temperature dependent proximity effect could lead to an increase in critical current. . . . . 48
- 3-1 Resistance versus temperature curves for NbN films with various sputtering conditions. The left inset zooms in on the superconducting phase transition, axis units are the same as main figure. The right inset shows the  $T_c$  as a function of  $RRM$  for each sample, where we see  $T_c$  decreases as  $RRM$  increases. The noise disparity between certain curves is due to the different measurement setups. Sample 1 in Table 3.1 refers to the bias sputtered film. . . . . 53

3-2 Left, thickness measurements of nitrogen rich NbN using a fixed angle ellipsometer. The solid blue line is a linear fit to the measured thickness where the slope is the resistivity, $\rho$ . The yellow line is the resistivity for bias sputtered NbN. Right, optical constants determined from multi-sample ellipsometer measurements [63]. At longer wavelengths, we see that the absorption coefficient $k$ is greater for nitrogen rich NbN. . . . .	54
3-3 Grazing incidence x-ray diffraction measurement of two NbN compositions. These results show an increase in the crystalline phases for the nitrogen rich NbN. The peak at 52° corresponds to the substrate. The blue curve was offset by an arbitrary amount for clarity. . . . .	56
3-4 High resolution top-down transmission electron micrographs. Left, bias sputtered NbN. Right, nitrogen rich NbN. Qualitatively, the bias sputtered NbN appears to be less crystalline than the nitrogen rich NbN, as there are fewer regions of visible lattice order. The scale bar is equal to 5 nm. . . . .	57
3-5 Selected area diffraction. Left, bias sputtered NbN. Right, nitrogen rich NbN. This measurement allows us to look at our material's reciprocal lattice. Here we see annular diffraction patterns that indicate the polycrystalline nature of our films. Additionally, we note greater definition in the two brightest rings for the nitrogen rich NbN and a rotational variation for the bias sputtered NbN. . . . .	58
3-6 Center profile of the selected area diffraction patterns. The blue curve has two distinct peaks at the (111) and (200) planes, while the yellow curve has a single peak at (200). Lattice planes were identified in Ref. [73]. . . . .	59
4-1 Scanning electron micrograph of two single photon detectors. The left image shows a 200 nm wide detector, meandered over $10 \times 10 \mu\text{m}$ area. The dark regions are the NbN film and the light region is the substrate where the NbN has been etched away, similarly for the right figure. The right figure shows a $3 \mu\text{m}$ wide detector in a straight configuration. The large meander below the detector is a series inductor to prevent latching. . . . .	64



4-5 Photon count rate curves for detectors of different width under 1550 nm illumination. The filled dots show the photon count rate normalized by the flattest region of the curve. If no plateau is present (i.e. 1.5 $\mu\text{m}$ & 3 $\mu\text{m}$ ) the counts were normalized by the maximum count rate. The solid lines are complementary error functions fit to the measured count rate. The right axis plots the dark count rate in kHz and is shown as crosses. The inset shows results of 0.5 $\mu\text{m}$ wide detectors with increasing series inductance. Each device was illuminated with the same optical power. The axis of the inset are in the same units as the main figure. . . .	72
4-6 Device jitter as a function of bias current and width. The left figure shows the full width half maximum of the measured jitter. Matching colors with Figure 4-5 correspond to the same device. The right figure shows the probability density function of the measured time difference between the laser pulse and the photon arrival. Each bias point was fit with a two term Gaussian distribution. The full width half max of each of the curves in the right plot correspond to the 1 $\mu\text{m}$ trend in the left plot. . . . .	74
4-7 Photon count rate curves for 3 $\mu\text{m}$ wide detectors at various wavelengths. The normalized PCR as a function of the constriction factor $C = I_{bias}/I_{dep}$ for the nitrogen rich film (dots) and the bias sputtered (crosses). Each curve of the nitrogen rich sample shows a saturated plateau. Dark counts for each measurement are plotted as squares. The inset shows the count rate as a function of attenuation for $\lambda = 1550 \text{ nm}$ and $I_{bias} = 0.43I_{dep}$ . . . . .	75
A-1 Comparison of critical temperature measurements as a function of width. Left, NbN samples measured at MIT. Right, critical temperature measurements of MoSi wires as a function of width, reprinted from [54] . . . . .	77

A-2 Statistical data for the critical current measurements at three temperatures. Box plots of the critical current deviation from the mean. The edges of the box plot represent the first and third quartiles and the center line in the box plot represents the median. Outliers are defined as measurements greater than one and a half times the inter quartile range. Color indicates unique devices. Measurements are normalized by the mean. The majority of measurements vary less than 10% from the mean. . . . .	78
A-3 Left, critical current measurements as a function of width. Distributions of critical current were performed at three temperatures and compared to baseline measurements using a Yokogawa GS200 current source. The critical current measured by the current source consistently returns a value lower than the distribution's mean. Each marker represents a unique device at a given temperature. Right, linear fitting to critical current measurements at three temperatures. As the temperature increases the intercept with zero critical current decreases; this indicates that the effective width of a wire is larger at higher temperature than at low temperature. A change in effective width supports the presence of a proximity effect. . . . .	79
A-4 Error in critical current measurements due to helium bubble formation. Left, two critical current measurements are plotted; one from the negative edge of the input ramp and one from the positive edge, for both temperatures. The low temperature data shows no correlation between positive and negative edges, while the high temperature data shows a periodic behavior. Right, the sum of the positive and negative critical currents is plotted for both temperatures. The low temperature data shows that the positive edge is typically higher than the negative edge. The high temperature data reveals the correlation between positive and negative measurements. . . . .	79
A-5 Timing jitter between laser and SNSPD pulse for four detectors. (a)-(d) correspond to $w = [1 \mu\text{m}, 1.5 \mu\text{m}, 2.5 \mu\text{m}, 3 \mu\text{m}]$ respectively. The color indicates the bias current relative to the critical current. The black lines are two term Gaussian distributions fit to the data. . . . .	80



# List of Tables

1.1	Table of saturated micrometer wide SNSPDs. . . . .	31
3.1	Table of NbN film properties. . . . .	52
4.1	Table of 200 nm wide SNSPD properties. Resistivity taken from fitting. . . . .	71



# Chapter 1

## Introduction

In this chapter we review the theoretical descriptions of superconductivity in thin films and single photon detection, as well as a review of the development of high-efficiency micrometer-wide single photon detectors. For the theoretical description, we begin with a classical description of superconducting charge carriers in bulk materials, followed by corrections to that theory for thin films. Next, we discuss modern descriptions of superconductivity, specifically, Bardeen-Cooper-Schrieffer (BCS) theory and Ginzburg-Landau theory. In the second section we review how superconducting theory applies to single photon detection in nanowires, and how those theories have evolved since their experimental discovery. Finally, a review of the experimental work towards micrometer wide single photon detectors is presented.

### 1.1 Theoretical description of thin film supercurrent

Superconductivity is one few macroscopic quantum mechanisms that lets us peer into the quantum world with our own eyes. The field of superconductivity has seen great balance between experimental discoveries—zero resistance [1], diamagnetism [2], and high-temperature superconductors [3]—and theoretical progress, from classical [4] to quantum [5,6] models. To maintain this balance as an experimental researcher, it is important to study the relevant theory. This section will not provide a complete review of superconducting theory but rather build the reader’s understanding towards the relevant theory for the experimental work. For a more complete review of superconductivity, see Refs. [7–10].

### 1.1.1 Macroscopic theory

The macroscopic theory of superconductivity was the first theory explain the electromagnetic behavior of superconductors. While the predictive ability of the model is incomplete, it is able to give us a general understanding of superconducting fields that can be probed in a laboratory setting. In this section we introduce the London equations and a thin film correction using a two dimensional treatment of Maxwell's equations.

#### London equations

In 1935, the London brothers described the electromagnetic behavior of bulk superconductors [4]. Their theory treated the electron condensate as free particles obeying Newton's acceleration law. They assumed that the drag (i.e. resistance) in the acceleration equation is zero, and following this assumption, they were able to describe the zero resistance and diamagnetic behavior (Meissner effect [2]) of superconductors for time-dependent magnetic fields. The first London equation (Eq. 1.1) is a material relation similar to Ohm's law  $\mathbf{J} = \sigma\mathbf{E}$ , where the electrons are accelerated with a static electric field. The next equation 1.2 (derived using the first London equation and Ampere's law) explains the diamagnetic properties of superconductors. However, these equations assume uniform fields and do not account for any spacial non-uniformity in realistic cases.

$$\Lambda \frac{\partial \mathbf{J}}{\partial t} = \mathbf{E} \quad (1.1)$$

$$(\nabla \times \mathbf{J}) = \frac{1}{\Lambda} \mathbf{B} \quad (1.2)$$

The London equations can be similarly derived using a quantum mechanical approach (Ref. [9] p.94). This approach, also published by F. London [11], assumed that the superconducting electron gas can be described by a macroscopic wave-function  $\psi(\mathbf{r})$  who's amplitude is normalized such that  $\psi\psi^* = n_s^*(\mathbf{r})$  where  $n_s^*$  is the superconducting electron density. The canonical momentum for this wave function is  $\mathbf{p} = m^*\mathbf{v}_s + e^*\mathbf{A}$ , where  $m^*$  and  $e^*$  are the effective mass and charge, respectively, and  $\mathbf{A}$  is the magnetic vector potential. The momentum in the ground state should have an expected value of zero; giving us a relation between  $\mathbf{A}$  a non-measurable quantity, and

$\mathbf{v}_s$  a measurable one. The average electron velocity  $\langle \mathbf{v}_s \rangle$  is measured as the current density  $\mathbf{J}_s = n_s^* e^* \langle \mathbf{v}_s \rangle$ . Leading to the London gauge<sup>1</sup>.

$$m^* \langle \mathbf{v}_s \rangle = -e^* \mathbf{A} \quad (1.3)$$

$$\Lambda \mathbf{J} = -\mathbf{A} \quad (1.4)$$

Where the parameter  $\Lambda = (m^* / n_s^* e^{*2})$ . Using the equality between the momentum density  $n_s^* \mathbf{p}$  and the expectation of the momentum operator  $\langle \psi | -i\hbar \nabla | \psi \rangle$ , we can prove that gauge selection only effects the local phase of the wave function, not a measurable quantity. The derivation of London equations using a simple quantum model, more specifically the proportional relation 1.4, shows that superconductivity is truly a quantum phenomenon [12]. Lastly, taking the curl of Ampere's Law for a static field  $(\nabla \times \mathbf{B}) = \mu_0 \mathbf{J}$  and  $\mathbf{B} = \nabla \times \mathbf{A}$  we get a Helmholtz equation for the vector potential  $\mathbf{A}$ .

$$\nabla \times \mathbf{B} = \mu_0 \mathbf{J} \quad (1.5)$$

$$\nabla \times (\nabla \times \mathbf{A}) = \mu_0 \mathbf{J} \quad (1.6)$$

$$\nabla \times (\nabla \cdot \mathbf{A}) - \nabla^2 \mathbf{A} = -\mu_0 \frac{\mathbf{A}}{\Lambda} \quad (1.7)$$

$$\nabla^2 \mathbf{A} = \frac{1}{\lambda^2} \mathbf{A} \quad (1.8)$$

Where we have employed the London gauge  $\nabla \cdot \mathbf{A} = 0$ . The eigenvalue of this Helmholtz equation is London penetration depth  $\lambda = (\Lambda / \mu_0)^{1/2} = (m^* / \mu_0 n_s^* e^{*2})^{1/2}$ . Similar equations for the current density  $\mathbf{J}$  and magnetic field  $\mathbf{B}$  can be derived however these three differential equations are good approximations for materials where the local relation Eq. 1.5 is valid [9]. In Figure 1-1 we numerically compute the vector potential (or current density assuming the London gauge) in two dimensional wire. We define Dirichlet boundary conditions of  $\mathbf{A} = 1$  at the edges, i.e. where the current will be maximum. We then solve Eq. 1.8 for multiple widths with a constant penetration depth of  $\lambda = 120$  nm. Taking a cut line through the center of the wire we can plot the local current density for each width. As the width increases the screening, or suppression in the center of the wire increases as more current is located towards the edges. We integrate over these

---

<sup>1</sup>In Sections 1.1.2 & 2.1, we consider the case where  $\Lambda$  not a constant.

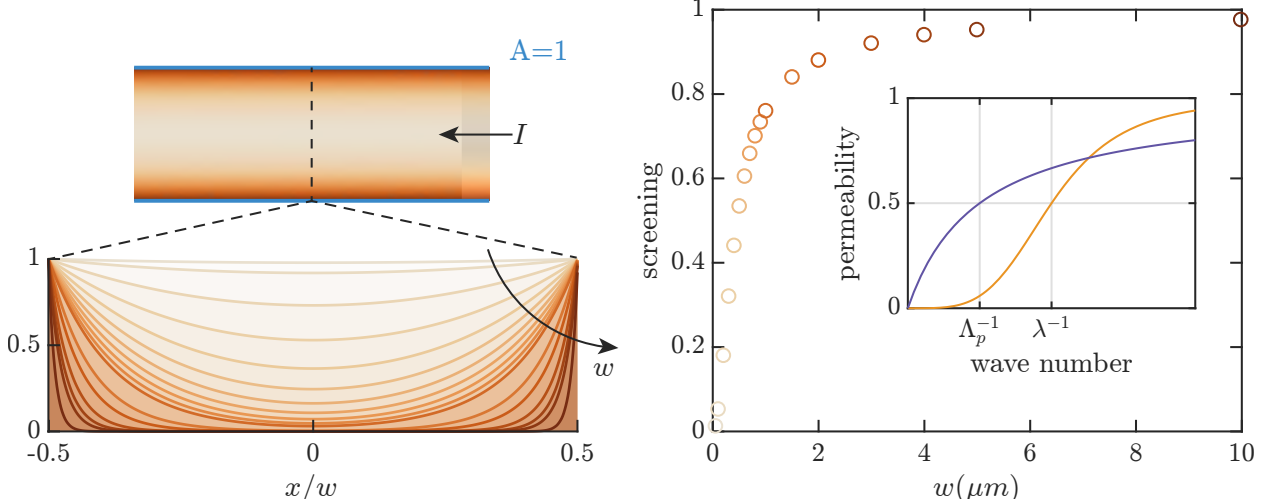


Figure 1-1: Numerical simulation of the vector potential in a two-dimensional superconducting strip. Left, a superconducting strip where the vector potential in the strip is equal to Eq. 1.8, and zero outside. Dirichlet boundary conditions define  $A = 1$  at the horizontal boundaries, corresponding to maximum current on the edges. For each width, a cut line (dashed line) was integrated to determine the amount of screening  $1 - \int J_c(x)/w$ . Right, the screening as a function of width. For the smallest widths the current distribution is near uniform and screening is zero. As the width increases the current is screened from the center. The inset plots Eq. 1.16 for the bulk and thin film case.

curves and normalize by the uniform current density to produce the screening versus width plot in Figure 1-1. The London equation predicts a saturation of current for strips much wider than the penetration depth; as the exponential decay towards the middle becomes infinitely small. This formulation will consistently underestimate the current in the wire as shown in Figure 2-1, due to increased permeability in thin films. A correction for thin films was presented by Pearl and is discussed in the next section.

### Pearl length

Pearl assumed an infinite sheet of superconducting material with a current loop  $\mathbf{J}_a$  in a parallel plane above it<sup>2</sup>. In order to repel the magnetic field generated by the loop, screening currents  $\mathbf{J}_s$  are allowed to form. Pearl knew for bulk materials these screening currents exist within a distance  $\lambda$  from the surface and supposed the current density for a thin film  $d \ll \lambda$  would be mostly uniform. The actual current distribution was replaced by an infinitely thin sheet  $\mathbf{J}_s^* = \mathbf{K}_s(\mathbf{r}_t)\delta(z)$ ,

<sup>2</sup>Where the plane extends infinitely over the  $\hat{x}\hat{y}$  plane in Cartesian coordinates. The film is of thickness  $d$  extending in the  $\hat{z}$  direction. A point in the film is defined  $\mathbf{r} = r_x\hat{x} + r_y\hat{y} + r_z\hat{z}$ .

where  $\mathbf{K}_s(\mathbf{r}_t)$  is the surface current. The surface current is defined as the integral of the actual screening current distribution over the film thickness.

$$\mathbf{K}_s(\mathbf{r}_t) = \int_{-d/2}^{d/2} \mathbf{J}_s(\mathbf{r}_t, z) dz \quad (1.9)$$

This allows us to solve the Maxwell-London equation  $\nabla^2 \mathbf{A} = -\mu_0 \mathbf{J}_{total}$  in two dimensions, where the total current is  $\mathbf{J}_{total} = \mathbf{J}_a + \mathbf{J}_s^*$ .

$$\nabla^2 \mathbf{A} = -\mu_0(\mathbf{J}_a + \mathbf{J}_s^*) \quad (1.10)$$

$$\nabla^2 \mathbf{A} = -\mu_0(\mathbf{J}_a + \mathbf{K}_s \delta(z)) \quad (1.11)$$

$$\nabla^2 \mathbf{A} = -\mu_0 \mathbf{J}_a + \frac{d}{\lambda^2} \mathbf{A} \delta(z) \quad (1.12)$$

Where we used the equation for Meissner superconductors  $\mathbf{J} = -\mathbf{A}/(\mu_0 \Lambda)$ . Taking the three dimensional Fourier transform from  $\mathbf{r}$  to  $\mathbf{q}$ .

$$(i\mathbf{q})^2 \mathbf{A}(\mathbf{q}) = -\mu_0 \mathbf{J}_a(\mathbf{q}) + \frac{d}{2\pi\lambda^2} \int_{-\infty}^{\infty} \mathbf{A}(\mathbf{q}) dq_z \quad (1.13)$$

$$\mathbf{A}(\mathbf{q}) = \frac{\mu_0}{\mathbf{q}^2} \mathbf{J}_a(\mathbf{q}) - \frac{d}{2\pi^2 \lambda^2 \mathbf{q}^2} \int_{-\infty}^{\infty} \mathbf{A}(\mathbf{q}) dq_z \quad (1.14)$$

Where we have used the sifting property of the delta function. Solving this integral equation returns wave vector dependent current terms:  $\mathbf{J}_a(\mathbf{q})$  and  $\mathbf{J}_s(\mathbf{q})$  (See Ref. [13] for details regarding this integral equation). Solving the permeability of the superconductor in the same manner as normal metals we can compute a wave vector dependent permeability.

$$\mu(\mathbf{q}_t) = \frac{\mathbf{J}_a(\mathbf{q}_t) + \mathbf{J}_s(\mathbf{q}_t)}{\mathbf{J}_a(\mathbf{q}_t)} \quad (1.15)$$

The permeability for bulk and thin film superconductors is

$$\mu_b(\mathbf{q}) = \frac{\mathbf{q}^2 \lambda^2}{1 + \mathbf{q}^2 \lambda^2} \quad \mu_f(\mathbf{q}_t) = \frac{\mathbf{q}_t^2 \lambda^2 / d}{1 + \mathbf{q}_t^2 \lambda^2 / d} \quad (1.16)$$

These functions are plotted in the inset Figure 1-1, where we see the characteristic length of the thin film permeability is less than the bulk material,  $\Lambda_p^{-1} < \lambda^{-1}$ . Inversely, the penetration of the magnetic field is greater in thin films  $\Lambda_p > \lambda$ , where  $\Lambda_p$  is the Pearl length.

$$\Lambda_p = \frac{2\lambda^2}{d} \quad (1.17)$$

This analysis could be constructed with two vorticies (see Section 1.1.2) with opposite rotation [14], where their interaction length would be the Pearl length.

London theory gives us a macroscopic electromagnetic model for superconductivity. It is able to predict the major observations from experimental research and Pearl's analysis is beneficial to thin film superconducting devices. However, London theory is only valid if local changes in the superconducting electron density  $n_s^*$  can be ignored. Additionally, London theory fails to account for type two superconductors, electron-phonon scattering, or phase transitions due to temperature or magnetic fields. We briefly discuss theories which address these properties in the next section and we present a quasiclassical model for thin film supercurrent in Chapter 2.

### 1.1.2 Microscopic theory

The microscopic theory of superconductivity has enabled every practical superconducting application. As it has been discussed in a number of textbooks [7, 9], this thesis will only present the equations and nomenclature necessary for the results shown in this thesis. This sections contains a description of the superconducting energy gap from BCS theory as well as the Ginzburg-Landau theory for type-II superconductors.

#### BCS theory

The microscopic theory of superconductivity of Bardeen-Cooper-Schrieffer (BCS) showed that the energy of a Fermi gas at zero temperature would be lowered if an attractive pair of electrons were added at zero temperature [5, 15]. At temperatures greater than zero, they predicted an energy gap  $\Delta(T)$  that separates the ground state of the paired electrons (Cooper pairs) and the

Fermi gas (unpaired electrons)<sup>3</sup>. The energy required to break a pair of electrons was predicted to be  $2\Delta(T)$ . Experimentalists confirmed the width of the energy gap by measuring the absorption of microwave and far-infrared photons [16]. In Chapters 3 & 4 we discuss how tuning the material parameters effect the energy gap and sensitivity to single photons. A useful approximation for the temperature dependence of the gap can be written for temperatures near  $T_c$ .

$$\frac{\Delta(T)}{\Delta(0)} \approx 1.74 \left(1 - \frac{T}{T_c}\right)^{1/2} \quad (1.18)$$

Where  $\Delta(0) \approx 1.76k_b T_c$ . BCS theory also provides an approximation for the temperature dependence of the penetration depth [7].

$$\lambda(T) \approx \lambda(0) \left[1 - \left(\frac{T}{T_c}\right)^4\right]^{-1/2} \quad (1.19)$$

### Ginzburg-Landau theory

So far we have either addressed both superconducting and normally-conducting electrons together classically, or just the superconducting condensate quantum mechanically. However, at temperatures above  $T = 0$ , where BCS theory is less accurate, not all of the electrons are participating in the flow of supercurrent [12]. A state where only a portion of the electrons are in Cooper pairs is called a mixed-state, and was presented in the theory by Ginzburg-Landau [17]. The total current is represented by wave function that is the sum of the dissipative current plus the non-dissipative current. The theory is then able to describe mixed state superconductors (i.e. type-II) that can support normal regions within a superconductor that allow magnetic field to penetrate. In a thin film, these regions are named vortices—small cores of normal regions surrounded by a circulating current—and initially form at defects, or constrictions in the material [18]. Vortex formation occurs most readily at these locations (due to the suppression of the superconducting wave function) but will appear throughout the film during any phase transition. The detection mechanism of SNSPDs is vortex-assisted and will be discussed Section 1.2.1.

---

<sup>3</sup>The wave function described the interaction of the paired electrons, however, the Fermi gas was considered classically.

## 1.2 Micrometer wide superconducting single photon detectors

In the past two decades, superconducting nanowire single photon detectors (SNSPDs) have been used in applications like neuromorphic computing [19], quantum key distribution [20], LIDAR [21], and dark matter detection [22, 23]. But since their first demonstration [24], a complete theory of detection has yet to be presented. Early models of detection in SNSPDs showed that the spectral cutoff of SNSPDs is inversely proportional to wire width. This indicated the width of the wire should be  $w \approx d_{hs} \ll 1\text{ }\mu\text{m}$  where  $d_{hs}$  is the diameter of a photon-generated hot spot. However, in 2017 a theoretical work [25] suggested micrometer wide SNSPDs would be sensitive to single photons, and was confirmed experimentally not long after [26–28]. Wide wire detectors<sup>4</sup> would increase the signal to noise ratio and ease the fabrication requirements compared to nanowires. Additionally, micrometer-scale features are readily patterned using photolithography, allowing for high-yield production in a foundry process. This would enable large area single photon detectors for applications with low photon flux such as deep-space communication [29] or dark matter search [22].

In this section we will review the development of micrometer wide SNSPDs. First, we present photodetection models and how they have evolved. Next we will describe how these models predict, or fail to predict, the single photon sensitivity of micrometer wide SNSPDs. Lastly, we will review the experimental evidence for wide SNSPDs and discuss their applications. As might be expected, this will be an incomplete description of the detection mechanism in SNSPDs. For that, we would direct to reader to Ref. [30].

### 1.2.1 Detection in micrometer wide wires

Early models of detection in SNSPDs gave an intuitive understanding of SNSPD operation and characterization. These models were limited in that they did not account for vortex-assisted detection. Time-dependent Ginzburg-Landau (TDGL) models of photodetection showed that detection is mediated by the creation of a vortex-antivortex pair. Applying kinetic-equation models

---

<sup>4</sup>Some have referred to wide detectors as SMSPDs, due to "nano" becoming "micro". We will continue to use SNSPD in this thesis for simplicity.

for the electron and phonon distributions, single photon sensitivity in micrometer wires up to a few micrometers wide were predicted [25]. We will discuss each of these models as it pertains to the experimental work in the later chapters.

### **Hot Spot Model**

The first experimental evidence of single photon detection in nanowires preceded a model for the mechanism of detection. The first theoretical model for photodetection was published by Semenov et al. [31] and is commonly referred to as the hot spot model, or its modified counterpart [32]. Photon detection within the hot spot model can be summarized as follows. Upon the arrival of the photon at the center of a superconducting strip, energy is absorbed into the material. This causes the growth of a normal region in the center of the wire and pushes the supercurrent into sidewalks on the edges of the film. If the current density in the sidewalks exceeds the critical current density then a completely normal region will form. This normal region produces a voltage pulse that is then read out using conventional electronics. With this model the current, wavelength, and temperature dependencies SNSPDs can be explained by variations of the hot spot model [33–36]. Because the size of the hot spot depends on photon energy and detection depends on the relative size of the hot spot to the wire width, there should be a cut-off of detection efficiency inversely proportional to width. Researchers have found this relation to be linear but ultimately showed that the hot spot model is unable to fully predict the gradual decay of detection efficiency beyond the cut-off [37].

### **TDGL and Kinetic-Equations**

The main problem with the hot spot model is that it assumes an immediate change in the superconducting order parameter, however we know this process to be up to the order of the electron-phonon relaxation time [38]. This leads to its inability to express the decrease in detection efficiency beyond the cut-off. This behavior was explained by vortex-assisted detection using the time-dependent Ginzburg-Landau (TDGL) theory [39]. Since then, more theoretical work focusing on the dynamics of electron and phonon distribution functions moments after photon absorption have been published [34, 40]. The pivotal work [25] which suggested micrometer wide SNSPDs, used the kinetic-equations to study the fraction of photon energy that gets transferred to

the electronic system. It showed that single photon detection in microwires requires the fraction of the electron versus phonon specific heat capacities being greater than one, and the maximum bias current being greater than 70 percent of the depairing current—the theoretical maximum current. In this regime, there is little geometric dependence in the current-energy relation. These conditions will be further discussed in Chapters 3 and 4.

$$\left. \frac{C_e}{C_{ph}} \right|_{T=T_c} \gtrsim 1 \quad I_{bias}/I_{dep} > 0.7 \quad (1.20)$$

In this work, the depairing current is calculated using an approximation valid for dirty superconductors [41, 42].

$$I_{dep}(0) = 0.74 \frac{w[\Delta(0)]^{3/2}}{eR_s\sqrt{\hbar D}} \quad (1.21)$$

Where  $\Delta(0)$  is the zero temperature energy gap,  $e$  is the electron charge,  $R_s$  is the sheet resistance,  $\hbar$  is the reduced Plank constant, and  $D$  is the electron diffusion coefficient (typically  $0.5 \text{ cm}^2 \text{ s}^{-1}$  for NbN). The temperature dependence is  $I_{dep}(T) = I_{dep}(0)(1 - (T/T_c)^2)^{3/2}$ . This approximate expression is sufficient for the use case presented here, however, more accurate models or experimental measurement of the depairing current could be used [43].

### 1.2.2 Experimental evidence

Following the theoretical work of Vodolazov [25], many were interested in demonstrating wide single photon detectors. In addition to the gains in fabrication and performance, developing materials suitable for wide wire detection implies that that material would be sensitive to longer wavelengths (mid-infrared) when patterned into nanometer wide detectors. In the first experimental demonstration [26], small bridges were patterned between 500 nm and 5  $\mu\text{m}$  and tested at 1.7 K and 4.2 K. The devices were kept short to prevent geometric degradation in the switching current and low-value shunt resistors were used to prevent latching. Each of these attributes are critical for wide wire operation in polycrystalline materials like niobium nitride (NbN). In other NbN works, researchers were able to improve the performance of their detectors using helium ions to reduce the superconducting gap [44].

The first demonstration in NbN prompted researchers to try fabricating wide detectors with

larger widths in different materials. However, nominal stoichiometric compositions of materials used for SNSPDs were unable to detect in wide geometries. For amorphous materials like MoSi [28] or WSi [27] the thickness was reduced and the silicon content was increased, two methods that reduce the superconducting energy gap. Unlike polycrystalline NbN detectors, large area detectors made from amorphous materials are less vulnerable to constrictions that result from grain boundaries.

Table 1.1 shows a complete list of published wide wire works, to the authors best knowledge. At the bottom of the table we list the properties of the device presented here. From this comparison, we find the NbN detector presented here is wider and more sensitive than previous NbN detectors. However, the amorphous materials have similar sensitivity and can be patterned into large arrays, making them more practical for most applications despite their low critical temperatures.

material	$d$ (nm)	$T_c$ (K)	$\rho$ ( $\mu\Omega\text{-cm}$ )	$w$ ( $\mu\text{m}$ )	$I_c$ ( $\mu\text{A}$ )	size <sup>b</sup> ( $\mu\text{m}^2$ )	$T$ (K)	$\lambda$ (nm)	institution
WSi	2.1	2.9	256.2	3	42	$100^2$	0.8	1550	NIST [27]
MoSi	3	3	175.5	3	25	$400^2$	0.3	1550	MIT [28]
NbN	7.5	9.1	385.5	1	228	$20^2$	1.7	1330	MPGU [45]
NbN	5.8	8.35	398.0	3	36.6	13.3	1.7	829	MPGU [26]
NbN	6.8	9	391.0	3	705	30	1.7	1064	MPGU [46]
NbN <sup>a</sup>	7	6.4	725.2	1	95	$50^2$	0.84	1550	SIMIT [44]
NbN	3.6	6.5	389.8	3	250	60	1.3	1550	MIT <sup>*</sup>

<sup>a</sup> Detector was exposed to helium ion irradiation to improve detection efficiency.

<sup>b</sup> Approximate size. Squared values are diameters of spiral detectors or side lengths of square meanders.

<sup>\*</sup> This work.

Table 1.1: Table of saturated micrometer wide SNSPDs.



# **Chapter 2**

## **Current Distribution and Reproducibility in Wide Strips**

In this chapter the theoretical model and experimental data for wide superconducting strips is presented. The theoretical model is a quasiclassical description based on the Usadel equations for dirty superconducting thin films. The model was developed by our collaborators, Dina Mazitova and Mikhail Skvortsov at the Skoltech Institute of Technology, and is presented here only for completeness [47]. The experimental section describes the nanofabrication process, cryogenic measurement setup, and noise contributions. The investigation of wires wider than the Pearl length is presented, as well as wires of increasing length, which allows us to characterize the effect of fabrication defects and material constrictions on the critical current.

### **2.1 Quasiclassical description**

In this section we review the quasiclassical model for dirty superconducting strips exceeding the Pearl length. The exact formulation of the model is beyond the scope of this thesis and this section will only present the relevant information needed to understand the experimental results. For more details regarding the model, we direct the reader to Ref. [47] or other references cited in this section.

Quasiclassical models have been long been applied to the theory of superconductivity [48]. These models allow for the fine structure of many body systems, which are often irrelevant for

practical applications, to be ignored. The first quasiclassical description, developed by Eilenberger, used Green's functions for impurity free systems at equilibrium [49]. Impurity free, or clean, implies that the elastic scattering rate  $1/\tau_{es}$  of the material is small compared to the superconducting gap  $\Delta$  and temperature  $T$  [50]. A large elastic scattering rate implies a high concentration of impurities, or a dirty superconductor (e.g. NbN). The quasiclassical model for dirty superconductors is referred to as Usadel's equations [51]. Solutions to these equations must be found numerically and the methods used to solve the system of equations will not be discussed.

In Section 1.1.1 we introduced a material relation between the current and vector potential  $J = -(1/\Lambda)A$ . This assumes that the material properties  $\Lambda$  are spatially constant and ignores any dependence on temperature or current. The first step of the model is to replace this constant value with a temperature and vector potential dependent kernel  $Q(T, A)$ .

$$J = -Q(T, A)A \quad (2.1)$$

The temperature dependence of the kernel  $Q(T, A)$  can be separated out and solved using BCS theory.

$$Q(T, 0) = \frac{\pi\sigma\Delta(0)}{\hbar c} \tanh \frac{\Delta(0)}{2T} \quad (2.2)$$

Where  $\sigma$  is the normal state conductivity. The kernel is then the product of this temperature dependence and a temperature and vector potential dependent function  $f_{T/T_c}(a)$  where  $a = A/A_c$ .

$$Q(T, A) = Q(T, 0)f_{T/T_c}(a) \quad (2.3)$$

The function  $f(a)$  is solved using the Usadel and self-consistency equations. After solving for  $f(a)$ , which is nonlinear and nonmonotonic, the material relation between  $J$  and  $A$  can be substituted into Maxwell's equation for current flowing in a thin strip.

$$\partial_x a(x) = \gamma(T) \int_0^1 \frac{f_{T/T_c}[a(x')]a(x')}{x - x'} dx' \quad (2.4)$$

In Eq. 2.4 we integrate the material relation over the width of the wire. Additionally, we introduce the dimensionless parameter  $\gamma = w/2\pi\Lambda_p(T)$ . This equation is solved assuming a boundary condition of  $a(0) = a(1) = 1$ , where the current reaches a maximum at the edges. The solution

to Eq. 2.4 is plotted in Figure 2-1 along with the solution from the London equations. The critical current is equal to the integral of each curve by definition. An approximation of the critical current as a function of temperature and width can be written (see Eq. 2.5 below) using two temperature dependent coefficients  $c(T)$  and  $\kappa(T)$ .

$$I_c(T, w) = \frac{j_c(T)dw}{\left[1 + \left(c^{-4}(T) + \frac{4\kappa(T) - c^{-4}(T)}{1 + 3\kappa(T)\gamma(T)}\right)\gamma^2(T)\right]^{1/4}} \quad (2.5)$$

The coefficients  $c(T)$  and  $\kappa(T)$  correspond to solutions in the wide and narrow width limits, respectively, and their temperature dependence is plotted in Figure 2-1. The approximate expression in Eq. 2.5 is the quasiclassical model referred to in the remainder of this chapter. To apply the model to experimental data one interpolates values of  $c(T)$  and  $\kappa(T)$  from the numerical results and replaces known material parameters specific to their experiment.

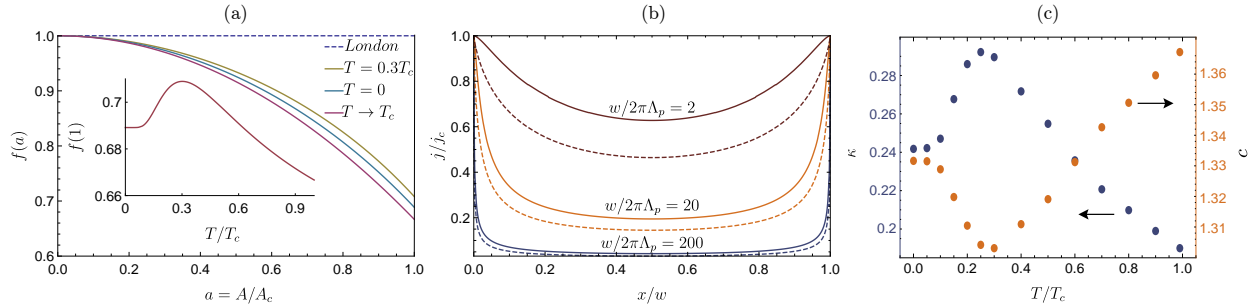


Figure 2-1: (a) The nonlinear, nonmonotonic material relation. Note this function is assumed to be constant in the London model. (b) Current screening in a superconducting strip. The dashed lines represent the screening determined by the London model. The solid lines represent the screening determined by the quasiclassical model. For each penetration depth shown the London model underestimates the amount of current in the strip. (c) The temperature dependent coefficients  $c(T)$  and  $\kappa(T)$ . Figures reproduced from [47].

## 2.2 Experimental setup

With a theoretical understanding of current through a superconducting strip, we investigate its predictive ability through experiments. The details of the performed experiment are critical for interpreting the observed results. In this section we discuss the fabrication and measurement of

superconducting thin strips.

### 2.2.1 Fabrication

This section will serve as a reference for the nanofabrication processes used to fabricate the devices presented in this thesis. The methods of fabrication are critical to superconducting elements as atomic discontinuities can cause degraded performance. Process times are reported here but fine tuning of each parameter is necessary for tools specific to the reader.

Thin film niobium nitride (NbN) was deposited by reactive sputtering in an AJA Orion system. Further detail on the sputtering process is described in Chapter 3. After depositing 5 to 20 nm of NbN, the sample is coated with electron beam resist. The choice of positive or negative tone resist depends on the application. For the devices mentioned in this thesis, positive tone ZEP520A or ZEP530A resist was spun at 5 krpm to a thickness of  $\approx$ 110 nm and baked at 180 °C for 2 min. The resist was then exposed using an Elionix 125 keV system with a 1 nm beam diameter. The applied dose was set to 500  $\mu$ C cm<sup>-2</sup> for ZEP520A or 550  $\mu$ C cm<sup>-2</sup> for ZEP530A. The beam current plays an important role on exposure time and edge roughness; resolution, however, is only slightly dependent on current and is mainly determined by the dose and development. For small features the minimum beam current of 500 pA was used and for larger features currents up to 40 nA was used to reduce exposure time. After exposure, the sample was developed in O-Xylene at a temperature of 5 °C for 90 s (ZEP520A) or 60 s (ZEP530A), followed by 30 s in isopropyl alcohol at room temperature.

Transferring the pattern in the resist to the sputtered NbN film is accomplished by reactive ion etching (RIE). The parameters used for etching are critical to fabricating a working device, as over—or under—etching can cause unwanted connections. A 10 min conditioning step of carbon tetrafluoride (CF<sub>4</sub>) and oxygen (O<sub>2</sub>) is run to remove residual contamination from the chamber. Next, the sample is placed in the chamber and pumped to a pressure of  $8 \times 10^{-5}$  Torr. CF<sub>4</sub> is then flowed in the chamber for 60 s at a pressure of 10 mTorr before the 50 W rf power is turned on and the plasma is sparked. Through calibration of the etch rate, it was determined that NbN is etched at a rate of 5 nm min<sup>-1</sup>. However, this etch rate was calibrated using unpatterned films and the etch rate of small trenches is nominally lower than that of full films due to the reactive ion's ability to bombard the small surface area. To ensure proper electrical isolation, it is possible

to probe the electrical resistance across a desired open circuit using either a multimeter or a micromechanical probe. If a resistance other than open is measured additional etching time can be added.

In the RIE system used, the temperature of the film's surface becomes sufficiently hot to burn the polymer resist, which hinders the ability to later remove the resist. A simple method to allow easy removal of the resist is to break the total etch time into segments <2 min long. This allows the sample to cool between etch cycles. The resist is then stripped in a heated bath of N-methylpyrrolidone (NMP) at 60 °C for 1 h. If possible, the sample is left in the NMP bath overnight at room temperature for complete resist removal; however, small amounts of residual resist do not effect device performance.

All of the devices shown in this thesis were fabricated at MIT either in the Nanostructures Laboratory or MIT.nano clean rooms.

### 2.2.2 Measurement

Cryogenic measurements combine electrical and thermal processes. Careful consideration of these processes, and how they influence nanowires, is the first step in performing an accurate measurement. This section will describe the measurement process used to evaluate the switching current as it relates to nanowire geometry.

The critical current ( $I_c$ ) of a wire is typically measured using a current bias and measuring the voltage across the nanowire. The current bias is achieved using a low noise voltage source (SRS SIM928) and a high value resistor (100 kΩ). The voltage is measured after the bias resistor with a Keithley 2700 multimeter.<sup>1</sup> When the wire is in the superconducting regime, a small resistance (< 5 Ω due to normal metal cables and wirebonds) is typically measured as the current bias is increased. When the bias exceeds  $I_c$ , the wire transitions into the normal state regime, producing a > 1 kΩ resistance.  $I_c$  is then defined as the largest applied current before the normal resistance forms. This method is suitable for quick  $I_c$  measurements but the accuracy of the recorded value is dependent on the step size of the applied dc voltage. Higher accuracy measurements can be achieved with a finer step size but this will increase the measuring time, quickly becoming im-

---

<sup>1</sup>This multimeter produces a significant amount of noise that can suppress  $I_c$ . To reduce this noise contribution a 1 MΩ resistor is placed in series with the input of the multimeter.

practical. Additionally, this measurement typically underestimates  $I_c$  due to the discrete current levels (Appendix A).

An alternative approach utilizes the high timing resolution of an oscilloscope. In this approach an arbitrary waveform generator (AWG) produces a triangular waveform that is split<sup>2</sup> evenly between the device and the oscilloscope. The bias resistor for the device is chosen to be  $50\Omega$  so that when the wire is superconducting each port of the splitter has matched impedance. When the wire transitions to the normal state, the large impedance mismatch produces a sharp jump in voltage on the oscilloscope. A typical oscilloscope trace can be seen in Figure 2-2. After the switching event, the measured voltage is no longer equivalent to the voltage across the device, due to impedance mismatch between ports of the splitter. However, for this experiment we are not interested in the voltage after the switching event. Instead, we use the captured waveform to extract the time between zero bias and the switching event. Using the time we can calculate the critical current using the slope of the applied waveform. In Eq. 2.6 the maximum current is simply the peak voltage  $V_p$ , times any applied attenuation  $a$ , over the resistance  $R$ , scaled linearly by the fraction of switching time  $t$  within one quarter period  $T$ .

$$I_c = \frac{V_p \times 10^{a/20}}{R} \left( \frac{t}{T/4} \right) \quad (2.6)$$

With this method a large number of  $I_c$  measurements can be captured in seconds. Additionally the accuracy of the measurement can be controlled by adjusting the sample rate of the oscilloscope (LeCroy 610ZI), up to 20 GS/s. However, waveforms with a millions of samples take longer to save and later process. Reducing the number of samples per waveform and capturing multiple waveforms allows us to work with smaller file sizes while capturing the small variations in the  $I_c$  that appear due to electrical or thermal noise, or the intrinsic stochastic behavior of nanowires [52].

This method allows us to quickly capture a large number of  $I_c$  measurements, but like any measurement method there are trade-offs to consider. The first trade off is that our bias resistor is lower than the nanowire resistance, meaning we do not have an ideal current source. The second is that the nanowire is transitioning from normal to superconducting states at the set

---

<sup>2</sup>Using a Mini Circuits ZFRSC-42B-S+ splitter.

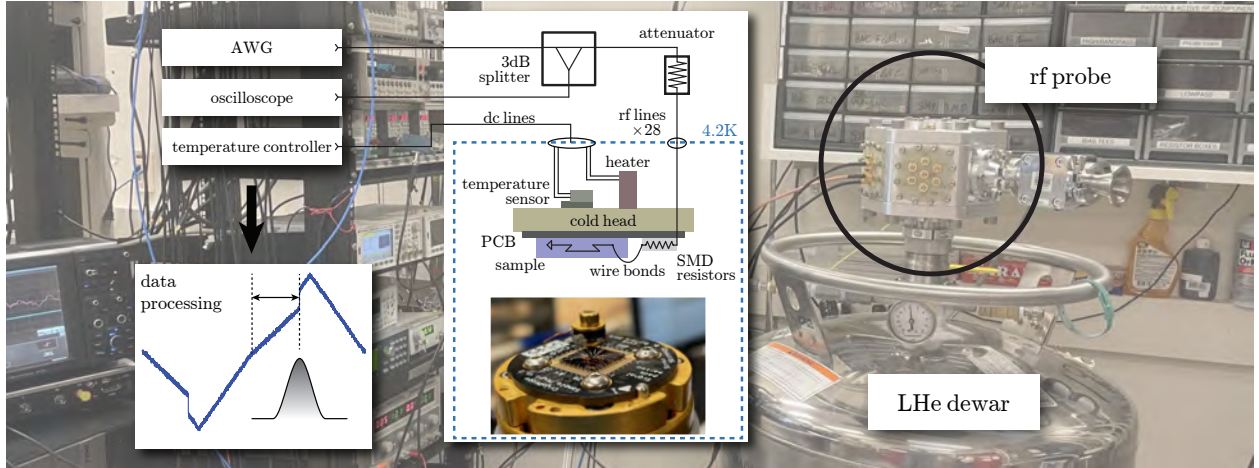


Figure 2-2: Typical setup for critical current measurements in liquid helium. Right, the rf probe immersed in liquid helium. Center, a schematic of the room temperature electronics and sample mounting. Left, the instruments used and a typical waveform of a nanowire biased beyond  $I_c$  with a triangular wave.

AWG frequency. If this frequency is too high, the change in voltage after switching is rolled off due to parasitic capacitance within our circuit. Additionally, if the nanowire spends the majority of the time in the normal state ( $t \ll T/4$ ) the local temperature will increase, causing a decrease in  $I_c$ . To abate this, the peak voltage was set such that the switching time remained constant: between 75 – 100% of  $T/4$ . The third trade-off is related to the threshold algorithm used to identify the switching time. A simple algorithm that triggers when the voltage exceeds a certain value can misidentify the switching event if the change in voltage is small, as is the case for wires with small  $I_c$ . The solution used here is to shift the recorded waveform in time by a fixed value and subtract the original from the shifted waveform. This produces an edge that is less dependent on the change in voltage, thus easier to identify when data processing. Lastly, this method works best for large currents ( $I_c > 20 \mu\text{A}$ ). For smaller currents the switching current is difficult to resolve from the noise floor and other characteristics, like the retrapping current  $I_r$ , are not visible.

## 2.3 Critical current measurements

Using the measurement setup described above we performed  $I_c$  measurements for various wire geometries. First we consider wires of a fixed width and measure the critical current as a func-

tion of length. This result later informed the design of wires of increasing width to investigate the critical current in wires exceeding the Pearl length. Finally, we compare the results to the quasiclassical model.

### 2.3.1 Length

In the lab we have observed, but not characterized, a reduction in critical current as the length of a wire increases. This is an important consideration when fabricating wires whose  $I_c$  should be only dependent on wire width. To characterize this, we fabricated two wires with alternating test point locations, thus creating a length-adjustable wire by changing the bias and ground points. Figure 2-3 shows scanning electron micrographs (SEM) of the measured devices. The left image

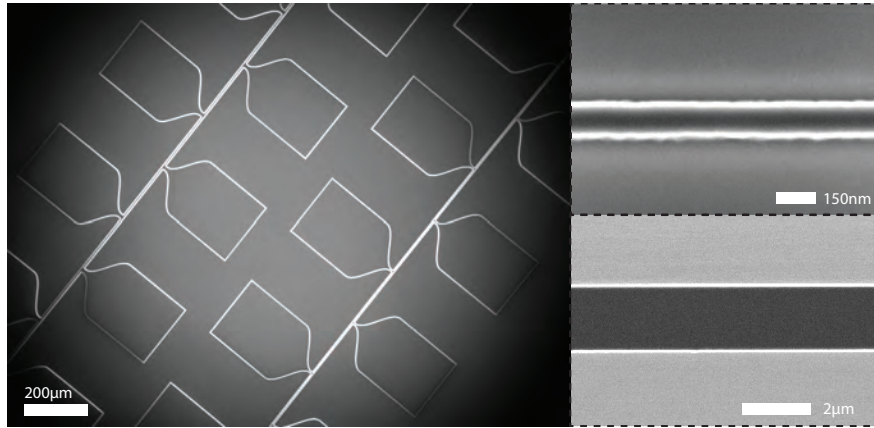


Figure 2-3: Scanning electron micrograph of two wires with test points spaced  $200\text{ }\mu\text{m}$  apart. The dark regions indicate the NbN film and the light gray regions indicate the substrate.

shows the two wires with alternating test points. The right images show high magnification images of each wire. For the narrow wire (150 nm), the edge roughness contributes to a larger variation in width relative to the designed width. The connections to the test points were made two times wider than the wire width and filleted to reduce current crowding. Current density simulations were performed to ensure the maximum current density occurred within the wire. Figure 2-4 shows the results of critical current measurements at each test point ( $tp$ ) for two widths. In the first experiment, an end pad ( $tp0$ ) was terminated with  $50\text{ }\Omega$  and a bias signal was applied to the next closest pad ( $tp1$ ). This was repeated for subsequent test points, keeping the ground terminated to  $tp0$ , in a 150 nm and  $2\text{ }\mu\text{m}$  wide wire. A total of 1000 measurements were performed

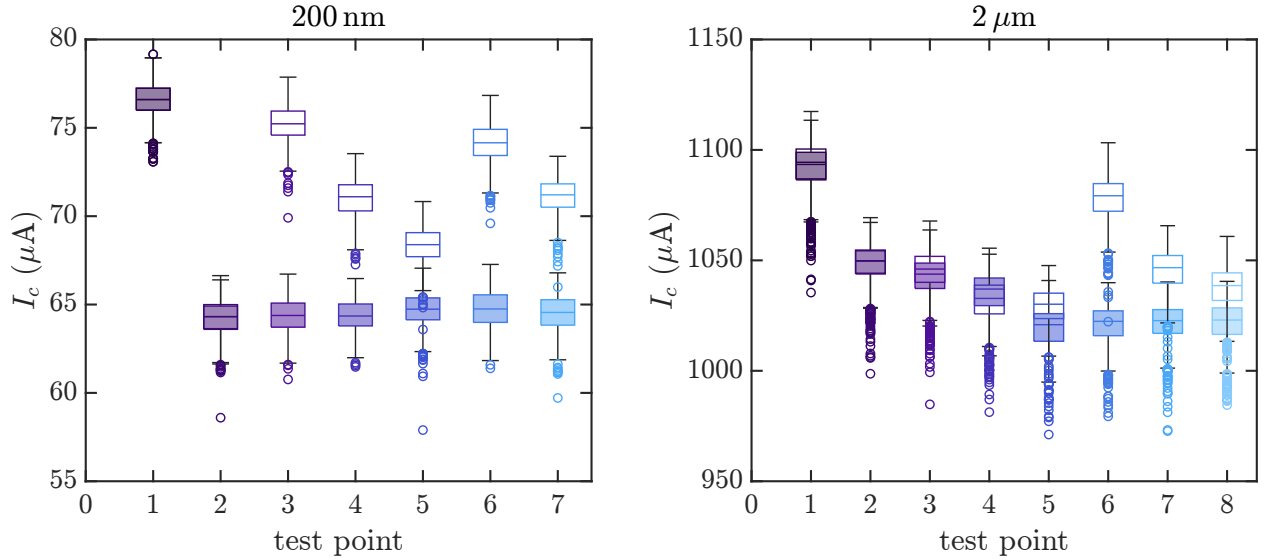


Figure 2-4: Critical current measurements at different test points. The filled box plot corresponds to measurements of increasing length, measured from the test point to zero. The empty box plots correspond to fixed-length measurements between adjacent test points. The empty boxes are less suppressed by cumulative constrictions along the wire.

for each test point using the methods described in Section 2.2.2 and are shown in box plots with filled boxes. Each measurement set had an average standard deviation of  $\sim 1 \mu\text{A}$  and  $\sim 10 \mu\text{A}$  for the 150 nm and 2  $\mu\text{m}$  wires, respectively. As the length of the wire increases, or as the test point number increases, the mean critical current falls.

In the second experiment, the distance between test points was kept constant, e.g. measure:  $tp_2$  ( $tp_1 \leftarrow tp_2$ ), ...,  $tp_7$  ( $tp_6 \leftarrow tp_7$ ). These measurements are plotted as empty box plots for each width. Clearly, the measurement  $tp_0 \leftarrow tp_1$  is the same for each experiment and the two box plots are nearly identical. For the remaining measurements in the 150 nm data set, the mean  $I_c$  was higher than the first experiment;  $tp_2$  was the exception, which had the same  $I_c$  as the first experiment. This shows that the most constricted segment is between  $tp_1$  and  $tp_2$ .

For the 2  $\mu\text{m}$  data set, a similar downward trend appears; although the most constricted section is  $tp_5$ , instead of  $tp_2$ . Comparing the results of each experiment, we can conclude that each wire has a segment that is more suppressed than others. The exact reason for this reduction is not directly apparent, though one might conclude that the critical current is reduced by material defects proportional to area.

### 2.3.2 Width

The majority of thin film superconducting devices assume homogeneous current distribution throughout the cross section of the wire. However, we know from the work by Pearl that if the width of the wire is similar to that of the magnetic penetration depth for thin films,  $w \approx \Lambda_p$ , the current will be localized to the edges of a wire [13]. This effect is an important consideration for the design of large scale superconducting circuits containing many elements and interconnects that span over a large range of widths. Additionally, the concentration of current density towards the edges could play an important role in photon detection, as high current density makes the wire more sensitive to incident photons. Inversely, edge concentration could suppress the switching current of a wire as the material is highly disordered at the edges, produced by bombardment of ions during the etch process or oxidation through the side walls.

The dependence of critical current density on wire width has been studied in NbN [53] and MoSi [54] films. In these works, wires sufficiently below the Pearl length are studied as lateral normal-superconducting-normal (NSN) proximity systems where the edges have suppressed superconductivity. However, these wires did not exceed the Pearl length and uniform current distribution in the superconducting portion was assumed.

To investigate the relation between switching current and width for wires that exceed the Pearl length, wires ranging between 50 nm and 100  $\mu\text{m}$  wide were fabricated. The length of each wire was fixed at  $2.5w$  to reduce suppression due to constrictions (Section 2.3.1). Details regarding the device fabrication and measurement setup can be found in Sections 2.2.1 and 2.2.2, respectively. We deposited a  $d = 23.3$  nm thick film with a Pearl length of  $\Lambda_p = 2\lambda^2/d \approx 5 \mu\text{m}$  (assuming a magnetic penetration depth of 250 nm for NbN).

In the first experiment we immersed the samples in liquid helium and measured the critical current of each wire. For each wire a total of 500 measurements were recorded and the mean value is plotted in Figure 2-5 for three temperatures. For a given temperature, each data point corresponds to a unique device<sup>3</sup>. The experimental data at 4.2 K was fit to the quasiclassical model using  $J_c$  and  $\Lambda_p$  as the only fitting parameters. The  $J_c(T)$  was determined by fitting to

---

<sup>3</sup>However, the specific device is not identified between temperatures, e.g. the four data points at 4.2 K and 60  $\mu\text{m}$  are the same devices as at 7.5 K and 60  $\mu\text{m}$  but the plot does not distinguish between the four devices. This was chosen to improve the clarity of the plot as the spread in values at a given width is small and more dependent on material and fabrication variations rather than measurement.

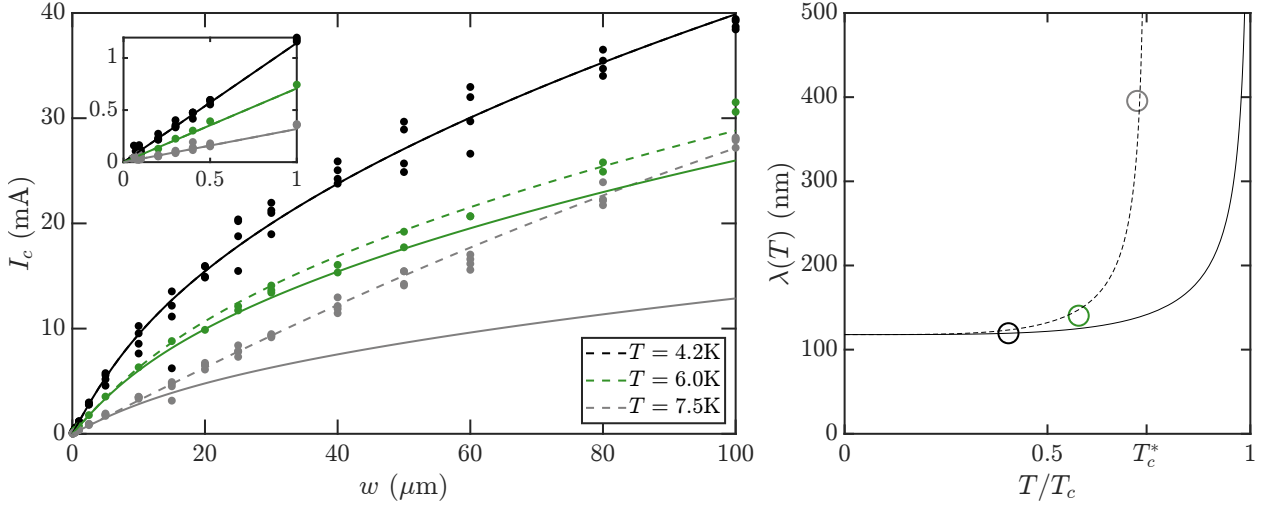


Figure 2-5: Left, average critical current of each wire at three temperatures. The solid lines predict  $I_c(w, T)$  with  $\lambda$  following the two fluid temperature approximation calculated from the fitting of the 4.2 K data,  $\lambda_{4.2}(0)$ . The dashed lines fit  $\lambda$  at each temperature, thus the solid and dashed curves for 4.2 K are identical. The inset shows the linear region  $w \ll \Lambda_p(T)$  with the same units as main axes. Right, The temperature dependence of  $\lambda_{4.2}(T)$  is plotted over the fraction of the critical temperature. The circles represent the penetration depth determined from the direct fitting (dashed lines in the left figure). The circles do not agree with the expected behavior  $\lambda_{4.2}(T)$ . To correctly predict the temperature dependence of the penetration depth a reduction in the critical temperature  $T_c^*$  is needed.

measured values in the linear region  $w \ll \Lambda_p(T)$ , which can be seen in the inset of 2-5. The result of the fit was  $\Lambda_p(0) = 1.18 \mu\text{m}$ . With this value we can determine  $\lambda(0)$  using Eqs. 1.19 & 1.17 and calculate the expected temperature dependence. The expected trend is shown in Figure 2-5 as a solid line. The agreement with the lowest temperature is expected from the fitting, but the deviation increases considerably as the temperature is increased. Similarly, that deviation can be seen in the right of Figure 2-5 as the error between the circles and the solid curve.

Another approach would be to try and fit to each temperature independently. The result of independent fitting is shown as dashed lines in Figure 2-5. On the left we see good agreement at all temperatures, but the trend on the right suggests a much lower critical temperature  $T_c^*$ . From this estimation  $T_c^* = 7.7 \text{ K}$ , which is lower than then the measured  $T_c = 10.4 \text{ K}$ . However, it has been shown that due to proximity effect the  $T_c$  can be dependent on the width for narrow superconductors [53, 54]. The  $T_c$  of each device was verified to be near 10 K and is included in Appendix A. A second explanation for the observed deviation could be a result of the measurement. Very frequently low temperature measurements can contain many sources of electrical and

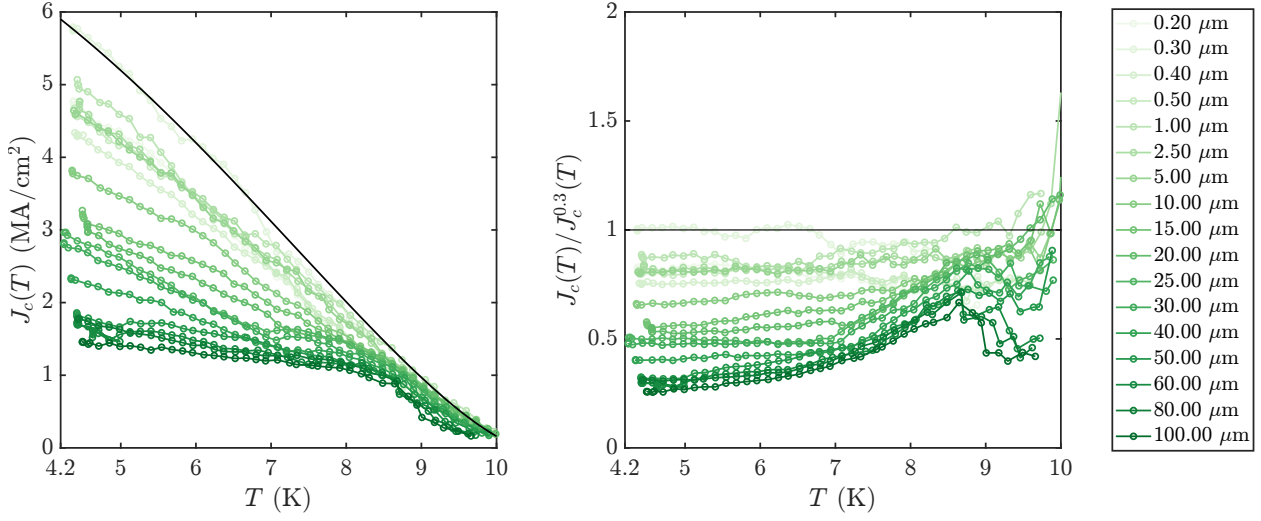


Figure 2-6: Left, temperature dependent critical current density for various widths. The black line was calculated from the highest critical current current measurement  $J_c^{0.3}$ . Right, the same data normalized by  $J_c^{0.3}$ . The  $0.3 \mu\text{m}$  wire is the least constricted while most narrow wires are clustered at  $0.8 J_c^{0.3}$ . As the width increases we see the current density is reduced. As the temperature increases  $J_c$  becomes less suppressed, and the gain is proportional to the width. Near  $8.5 \text{ K}$ ,  $J_c$  starts to decrease, returning closer to the expected temperature dependence.

thermal noise. However, this is unlikely to explain our observations, as noise will only suppress  $I_c$ . Additionally, we performed statistical analysis of each measurement, as well as making comparisons with two different measurement setups. The results from this investigation are shown in Appendix A.

A third explanation is that there is an additional physical process not being captured by the model. If this is a true feature of the device, and not due to measurement error, the increased  $I_c$  should be visible when doing temperature dependent sweeps of  $I_c$ . To verify this, we performed temperature dependent sweeps of devices  $\geq 200 \text{ nm}$  wide—the smallest wires were excluded from this measurement as the voltage change at high temperatures can be indistinguishable from the noise floor. The same measurement procedure was repeated at many temperatures up to  $T_c$  using an integrated temperature sensor and heater [55]. The sample is well thermally coupled to the sensor (Lakeshore DT-670) which is calibrated to  $1.4 \text{ K}$ . The relative placement of the sensor and heater is shown in Figure 2-2.

The temperature was then set using a programmable temperature controller (Cryocon 34). The measured temperature was recorded before and after each data collect and had  $< 0.05 \text{ K}$  variation for all measurements. The resulting curves are plotted in Figure 2-6. For the highest

recorded  $J_c$ , we calculated the full BCS temperature dependence of  $J_c$  using Eq. 2.7 [7]. This measurement and the temperature dependence is plotted Figure 2-6.

$$J_c(T) = J_c(0) \left( 1 - \left( \frac{T}{T_c} \right)^2 \right)^{3/2} \quad (2.7)$$

In Figure 2-6 (left) we see the region where the critical current was higher than predicted (recall Figure 2-5). To compare this data to the experiment shown in Figure 2-5 we interpolated over the measured widths at 6 and 7.5 K (dashed lines). The interpolation is shown in the inset of 2-6. Smoothing the interpolation results in solid curve and the shaded region corresponds with the shaded region in Figure 2-8.

In the right of Figure 2-6 there are two interesting behaviors. First is the large increase in  $J_c$  for the widest wires. There is an expected increase due to the change in  $\lambda(T)$ , however, not to the degree observed. Quantitatively, the largest increase is equal to a 30% gain in the constriction factor  $C = I_c/I_{dep}$ , which is expected to decrease near  $T_c$  [43]. Instead,  $C$  reaches a maximum at 8.5 K. The second interesting behavior is the inflection at  $\approx 8.5$  K. Here, the widest wires have the sharpest decent, while for wires  $w \approx 20 \mu\text{m}$  the slope is more positive.

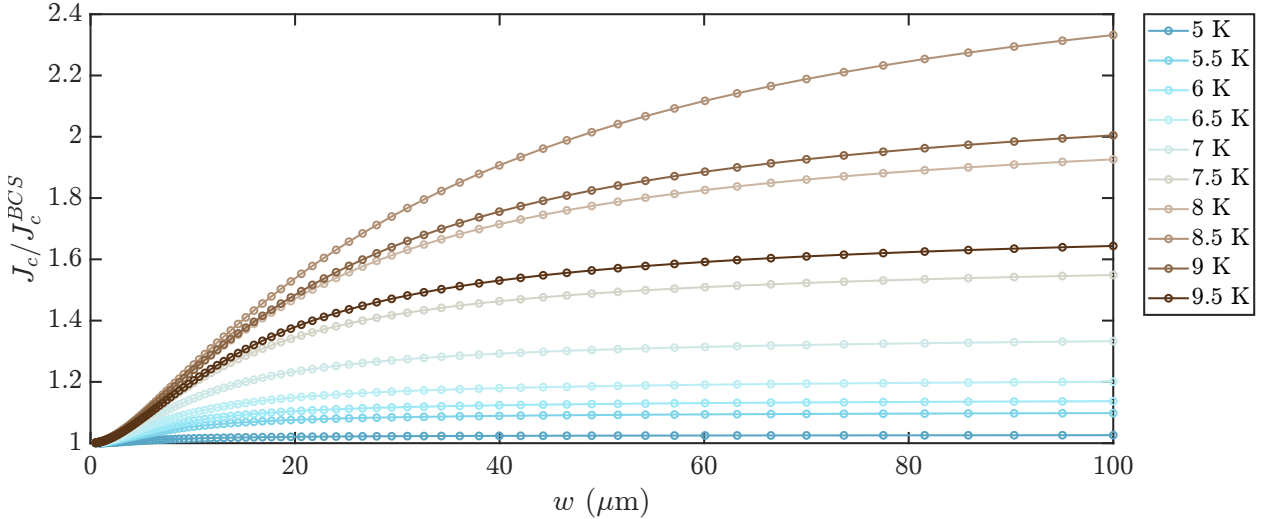


Figure 2-7: Interpolated data from the measured data in Figure 2-6. The change in the critical current density relative to the expected temperature dependence as a function of width and temperature. This used as a correction factor to the quasiclassical model.

To simplify further analysis, the data was interpolated over the temperature and width axes.

The result of this interpolation, relative to the expected  $J_c$ , is plotted in Figure 2-7. After the interpolation, the nonmonotonic behavior with temperature is clear. With this dataset, we confirm our previous measurements by introducing a correction factor. This can be thought of as either an effective width of the wire  $w^*$ , or a width-dependent current density  $J_c(T, w)$ . After fitting with the correction, we find improved agreement with the temperature dependence of the penetration depth at 6 K and a slight improvement at 7.5 K. The contribution of the correction coefficient is shown in Figure 2-8 as shaded regions between dashed and solid lines.

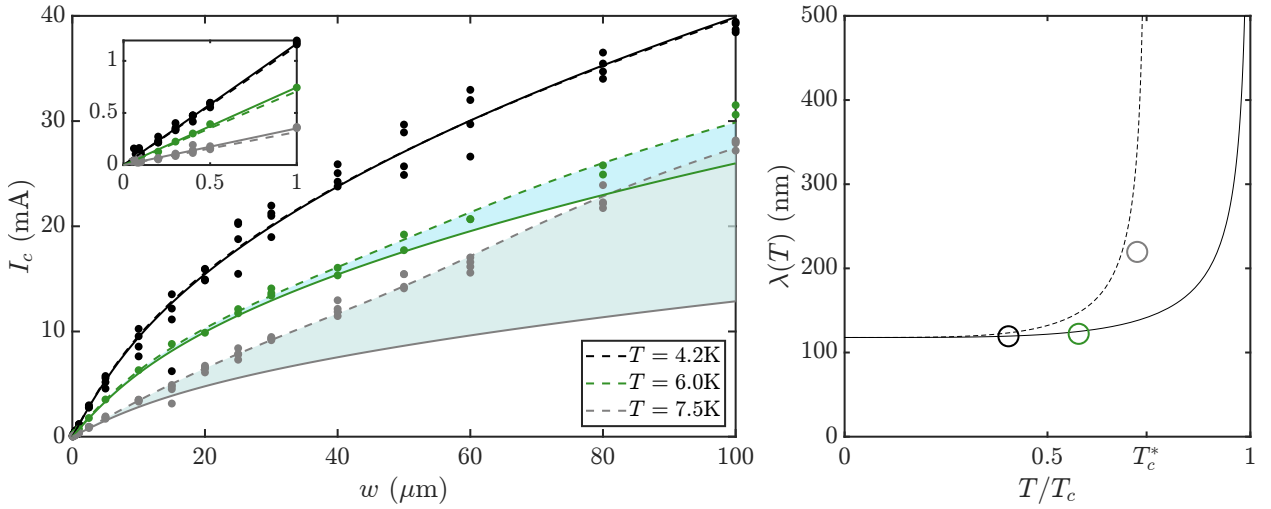


Figure 2-8: The predicted  $I_c$  from the quasiclassical model with the  $J_c$  correction coefficient. This figure is identical to Figure 2-5 but with the correction shown in Figure 2-7. Left, the solid lines show the expected temperature dependence calculated from the 4.2 K data. The dashed lines represent the fit of the quasiclassical model with the correction coefficient. The correction coefficient is depicted as that shaded region between the dashed and solid lines. Right, the penetration depth determined from the quasiclassical model. With the correction,  $\lambda(T)$  now aligns with the expected trend.

So far we have looked at two data sets. The first measured wires of different widths at three fixed temperatures and the second performed temperature sweeps on those same wires. Using the second data set, we extracted a width and temperature dependent correction factor. Applying the correction factor to the quasiclassical model improves the predicted temperature dependent penetration depth when fitting to the first data set. The same procedure can be performed on the second data set, as shown in Figure 2-9, however this is recursive and is only used to aid in visualization.

This section has shown that the quasiclassical model is unable to predict the temperature

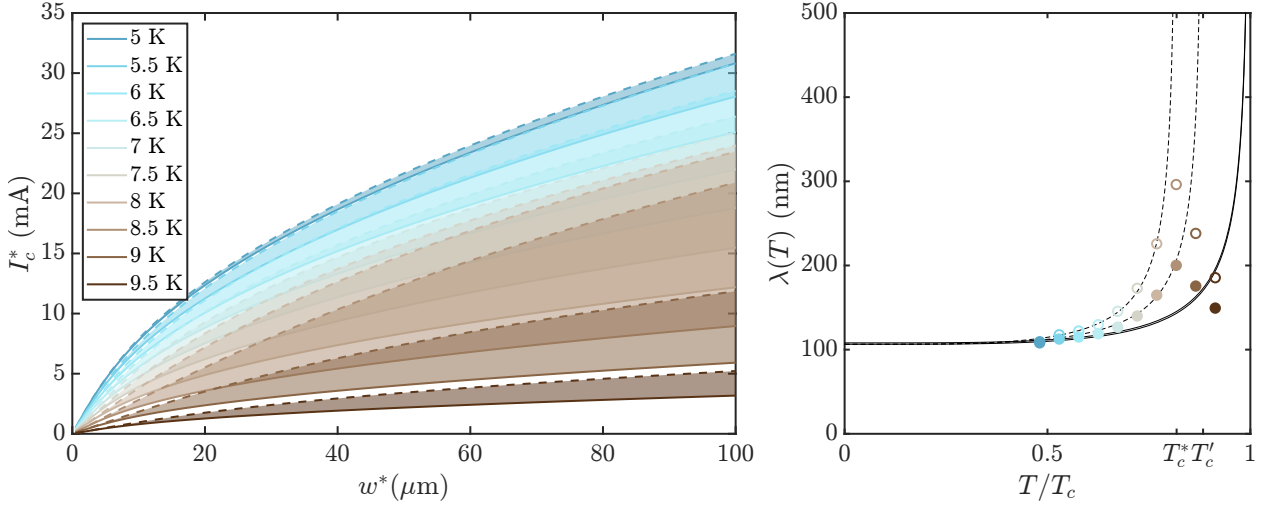


Figure 2-9: Predicted critical current using the interpolated temperature sweep data. Left, the solid lines show the expected BCS temperature dependence. The dashed lines show the fitted temperature dependence with the correction coefficient (shaded region). Right, the penetration depth of the interpolated data without the correction (circles), and the corresponding effective critical temperature  $T_c^*$ , and the penetration depth with the correction (dots),  $T'_c$ . The solid line shows the expected temperature dependence.

dependence of the penetration depth with a  $J_c(T)$  determined fitting to the narrow wires. We measured the  $J_c(T)$  of wires 200 nm and wider and found  $J_c(T)$  did not follow the expected temperature dependence  $J_c^{BCS}$ . The ratio of the measured critical current density to the expected BCS value  $J_c(T)/J_c^{BCS}$  is used as a correction factor to the quasiclassical model, replacing the assumed value of  $J_c(T)$  from narrow wires. This improves the resulting penetration depths, however there is still disagreement between the quasiclassical model and the BCS temperature dependence.

The exact reason for the observed behavior is not understood. Here we will present our conclusions and present future work. The model without any correction correctly predicts  $\lambda(T)$  for the first few, and final, temperatures. However the values near  $0.8T_c$  are much higher than expected, resulting in effective critical temperatures,  $T_c^* = 8.5$  K and  $T'_c = 9.2$  K, lower than the measured value  $T_c = 10.4$  K. The lower effective critical temperature could be due to the applied bias current. The current through a superconducting strip can suppress the critical temperature when near  $I_c$  [56]. When measuring the critical temperature, the bias current was set to  $I_b < 0.1I_c$ . However, during the bias ramp of a  $I_c$  measurement, the current flowing through the wire prior to switching could potentially effect the  $T_c$ . A measurement similar to the one in Ref. [56] would

be beneficial.

An effective change in width might also explain the observed behavior. In narrow wires, there is evidence of a proximity effect in the edges of the wire [53, 54]. The results presented in these works deal only with ultra narrow wires, where they observe a change in  $T_c$  as a function of width. While we do not observe a change in  $T_c$ , we note that the proximity effect is modeled as a NSN system, where the width of the superconducting region is  $w^*$ . At a point  $|x| > w^*/2$  the superconducting order parameter decays into the normal region. In the narrow wire case, the current at  $|x| < w^*/2$  is assumed uniform, resulting in the dashed line in Figure 2-10. In the wide wire case, the central current will be screened proportional to  $w^*$  opposed to  $w$ . Under these conditions, the integral of  $J_c$  along the width of the wire would increase. This effect is exaggerated for clarity in Figure 2-10. Further investigation is needed to confirm any of the hypotheses above.

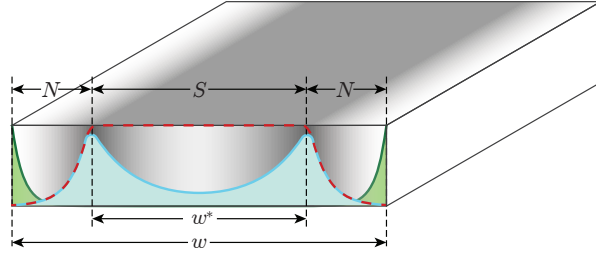


Figure 2-10: A cross section of a thin superconducting strip wider than the Pearl length. The solid blue line, maximum at NS boundary, combines the suppression in the center of a wire due to the Pearl length screening and the decay to the edges due to the proximity effect. Its integral, shaded in blue, is greater than the distribution of current extending over the entire width, shaded in green. The red dashed line represents the proximity effect in a wire modeled as a normal-superconducting-normal (NSN) lateral stack. A temperature dependent proximity effect could lead to an increase in critical current.

# Chapter 3

## Nitrogen Rich Niobium Nitride

In this chapter we perform a material study of niobium nitride (NbN) thin films. By investigating the atomic structure of NbN, we hope to learn what composition and phase is suitable for wide wire detectors. We begin with an introduction to thin film deposition by reactive sputtering and describe the parameters of interest. Thin films were sputtered under various conditions and electrically analyzed before two films were selected for further characterization. To better understand the microscopic structure of the two NbN films, we analyzed each sample using x-ray diffraction and transmission electron microscopy.

### 3.1 Introduction

In reactive sputter deposition, atoms from a target are ejected into an atmosphere of a reactive gas and deposited on a sample [57]. In our case, a high-purity niobium target is sputtered in a reactive atmosphere of nitrogen. The resulting NbN stoichiometry depends on the temperature, pressure, gas flows, power, deposition time, substrate, and working distance. Given a desired characteristic (e.g.  $T_c$  [58]) the deposition parameters can be varied to maximize the given characteristic. This method was used to develop room temperature bias sputtered NbN, a material that has  $T_c$  similar to NbN deposited at high temperature [59]. Using the bias sputtered NbN, micrometer wide detectors were unable efficiently detect 1550 nm photons, indicating the need for material engineering. Before varying any parameters, we will identify characteristics that are important to wide SNSPD development.

As mentioned in Chapter 1, developing materials for wide SNSPDs is centered around reducing the superconducting gap, increasing the electron specific heat capacity  $C_e/C_{ph}|_{T=T_c} \geq 1$ , and increasing the bias current to greater than 70% of the depairing current [25]. All three criteria are dependent on the material characteristics, however the maximum bias current is also limited by the device fabrication [43] and will receive greater attention in Chapter 4. The superconducting gap at zero temperature is approximately proportional to the critical temperature,  $\Delta(0) = 1.76k_b T_c$ , which we can reduce by using a thinner film. Thus, a thinner film should be more sensitive to low energy photons. As a starting point, we fabricated wide SNSPDs from ultra thin ( $\approx 2\text{-}3$  nm) bias sputtered NbN and found that the detector could only reach 20% of  $I_{dep}$ . We attribute this to an increase in film discontinuities for polycrystalline films with thickness comparable to the substrate surface roughness. Amorphous films could be made into micrometer wide detectors by growing ultra thin films ( $\sim 3$  nm) [27, 28].

To better understand the material differences, we compare the composition of our bias sputtered NbN with the composition of NbN used in Ref. [26], which we refer to as nitrogen rich NbN. Both compositions fall into a category of superconductors called marginal superconductors [60, 61]. A marginal superconductor is one that has high resistivity (compared to that of metallic superconductors) and has a resistivity dependent  $T_c$ . In metallic superconductors, the resistance decreases as the sample is cooled down—due to a reduction in electron-phonon scattering—before the superconducting transition reduces the resistance to zero. At low temperatures, prior to the superconducting transition, the residual resistance is primarily due to grain boundaries or impurities in the material. The residual resistance ratio  $RRR = (R_{300} - R_{4.2})/R_{4.2}$  is used characterize the metallic  $RRR > 0$  or non-metallic  $RRR < 0$  behavior of the material. The behavior of NbN is strongly non-metallic and its effect on the superconducting properties is not fully understood [62]. However, the superconducting-insulating transition is related to a reduction in the energy gap  $\Delta$  and phase coherence  $\phi$ . To investigate these materials, one might use a new ratio  $RRM = R_{max}/R_{300K}$  proposed by Zolotov et al. [61] to measure the degree of marginality. The remainder of this chapter will be devoted to investigating how these properties are effected by the sputtering parameters. Parameters for increasing the  $RRM$  while maintaining a reasonably high  $T_c$  to allow for operation in liquid helium are studied.

## 3.2 Electrical and optical characterization

In this section we deposit thin films of NbN with various sputtering conditions. As a starting point, we set the deposition parameters to match those used in Ref. [26]. From there, we varied the nitrogen ( $N_2$ ) and argon (Ar) flow rates and the deposition temperature. All other parameters were kept constant. After each deposition, the sheet resistance was measured using a four-point probe. Measuring directly after removal from the vacuum chamber is necessary as NbN is known to form an oxide,  $Nb_2O_5$ , which can cause an increase in the measured resistance over time [63]. Furthermore, this change in sheet resistance is often a source of error if it is used to calculate the thickness or resistivity. Still, sheet resistance is the more commonly used parameter when discussing superconducting thin films, as it is generally a good estimate.

The ratio of the nitrogen and argon flow rate influences the ratio of N and Nb in our film, respectively. When increasing the nitrogen content we expect the resistance to increase as the film becomes less metallic. We see this between samples 2 and 3 in Table 3.1. Sample 4 is expected to have higher resistance, however it is lower resistance than 3. This likely due to the flow rate of  $N_2$  being at the maximum set point for our system, thus not accurately increasing the  $N_2$  content. In sample 5 we reduce the Ar flow rate, reducing the Nb content, however the resistance is similar to that of sample 3. We can note that the deposited thickness is lower, as the deposition rate is controlled by Ar, which leads to a higher resistance. As films become extremely thin, the resistance increases non-linearly. An example of this large increase is visible between samples 6 and 7 where two films were deposited under identical conditions, with the exception of a 10 s difference in sputtering time. The deposition temperature adds thermal energy to the atoms, increasing crystalline order and reducing resistance (e.g. see table entries for samples 2 and 8). An observant reader would note that the resistivity actually decreased between those two samples, further highlighting the need to determine the resistivity of a material using multiple samples.

From the results in Table 3.1 the film composition which is likely to have the greatest sensitivity to single photons in micrometer SNSPDs is sample 7, due to the high  $RRM$  and low  $T_c$ . However, the critical temperature is close to that of liquid helium  $T = 4.2$  K. This removes any operational advantage one might have using NbN opposed to lower  $T_c$  materials which requires high performance cryostats. For that reason, we will continue to use the composition of sam-

ple 8 [26]—which has higher  $T_c$  and  $RRM$  than sample 1—and perform further analysis of the material with respect to our bias sputtered NbN. From the simple comparison of the  $N_2/Ar$  ratio, sample 8 has 50% more  $N_2$  than sample 1, however the bias and current conditions can also effect the final composition. Accurate composition analysis could be performed using a direct measurement method (e.g. atomic probe tomography [64]).

sample	$N_2$ (sccm)	Ar (sccm)	$T$ (°C)	current (mA)	$R_s$ (Ω/sq)	$d$ (nm)	$\rho$ ( $\mu\Omega\text{-cm}$ )	$T_c$ (K)	RRM
1 - SPG361	6	26.5	20	400	348.6	5.30	184.8	7.57	1.48
2 - SPG451	14	40.0	800	550	790.2	3.53	278.9	7.38	1.60
3 - SPG452	18	40.0	800	550	979.4	3.16	309.5	6.16	1.79
4 - SPG453	20	40.0	800	550	965.2	3.08	297.3	6.50	1.78
5 - SPG457	18	25.0	800	550	979.2	2.94	287.8	6.71	1.71
6 - SPG477	18	40.0	500	550	836.1	3.41	285.1	6.15	1.89
7 - SPG484	18	40.0	500	550	1295.3	3.10	401.5	4.99	2.00
8 - SPG371	14	40.0	500	550	549.3	4.37	240.0	7.79	1.71

Table 3.1: Table of NbN film properties.

The  $T_c$  and  $RRM$  of each sample in Table 3.1 was determined from the resistance vs temperature measurements shown in Figure 3-1. The resistance of each sample was repeatedly measured in a four-point probe configuration as the temperature was lowered. The noise variation between measurements (e.g. between 1 and 2) is due to the measurement apparatus used<sup>1</sup>. In the low noise case, the samples were mounted in a custom built dip probe and measured at a frequency of 2 Hz as the sample was manually lowered into liquid helium. In the high noise case, the sample was measured using a closed-cycle cryostat which samples the data much faster than the cool down rate. Additionally, there is vibrational noise from the coldhead motor which causes local displacement of contact pins. From these curves the  $T_c$  was taken to be the temperature where the resistance reaches 50% of the max resistance  $0.5R_{max}$ , and  $RRM = R_{max}/R_{300K}$  [61]. The inset in the lower left zooms into the superconducting transition. We can see sample 3 did not completely transition to the superconducting state, however the minimum resistance was less than  $0.5R_{max}$ . The inset in the upper right we see the relation between  $T_c$  and  $RRM$ . There is a gen-

<sup>1</sup>Additionally, the measured resistance is different between apparatus due to source and contact variations. The relative change in resistance is the parameter of interest in this case, and this variation was deemed negligible.

eral downward trend in  $T_c$  as  $RRM$  increases, other than sample 8 where we are able to increase the  $RRM$  while maintaining the  $T_c$ . As stated, sample 7 would have the smallest superconducting gap, making it the best candidate for wide wire detection, but the decreased  $T_c$  reduces the probability of yielding a working detector above liquid helium temperatures. For those reasons, we continue to investigate sample 8 and future references to nitrogen rich NbN will refer to this composition.

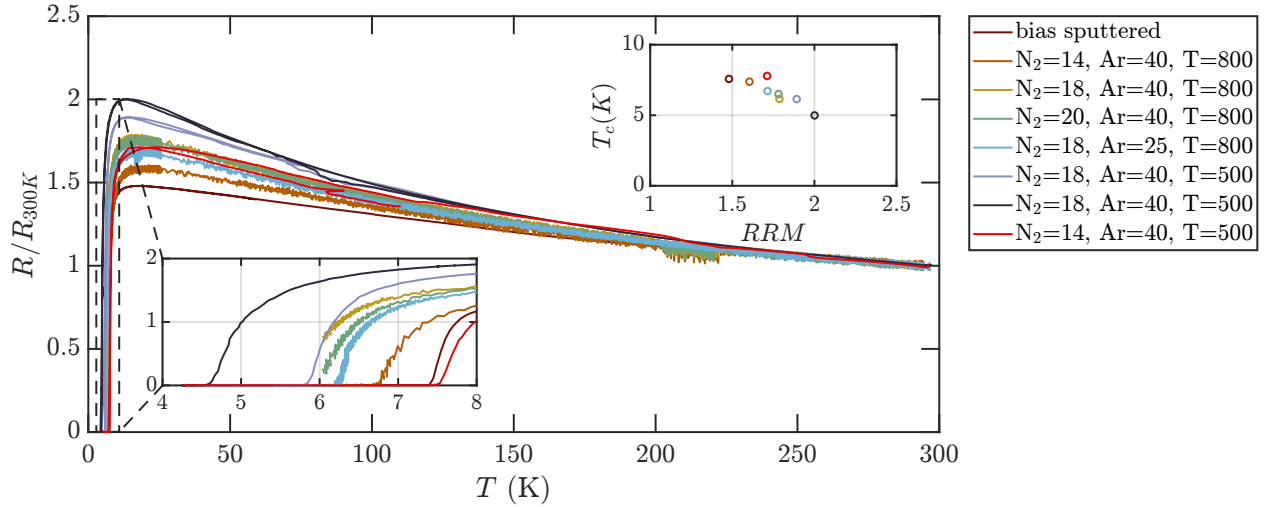


Figure 3-1: Resistance versus temperature curves for NbN films with various sputtering conditions. The left inset zooms in on the superconducting phase transition, axis units are the same as main figure. The right inset shows the  $T_c$  as a function of  $RRM$  for each sample, where we see  $T_c$  decreases as  $RRM$  increases. The noise disparity between certain curves is due to the different measurement setups. Sample 1 in Table 3.1 refers to the bias sputtered film.

The nitrogen rich composition (sample 8) was further studied by depositing films of different thickness. Having multiple thicknesses lets us more accurately characterize the material's resistivity and lets us build an optical model using multi-sample analysis [63]. Figure 3-2 shows the results of the film resistivity and optical constants. The left figure shows the linear fitting of the thickness  $d$  versus the sheet conductance  $R_s^{-1}$ . This results in a resistivity of  $389.9 \mu\Omega \text{ cm}$  for the nitrogen rich NbN, which is a 60% increase compared to the bias sputtered NbN, determined in Ref. [63], which closely matches the 50% increase in the  $N_2:Ar$  ratio. Using these samples we are able to construct an optical model of our material using a fixed angle ellipsometer (Film Sense FS-1). The results of both materials are shown in the right of Figure 3-2. For the given wavelengths, we plot the real and imaginary components of the refractive index for each material. At longer

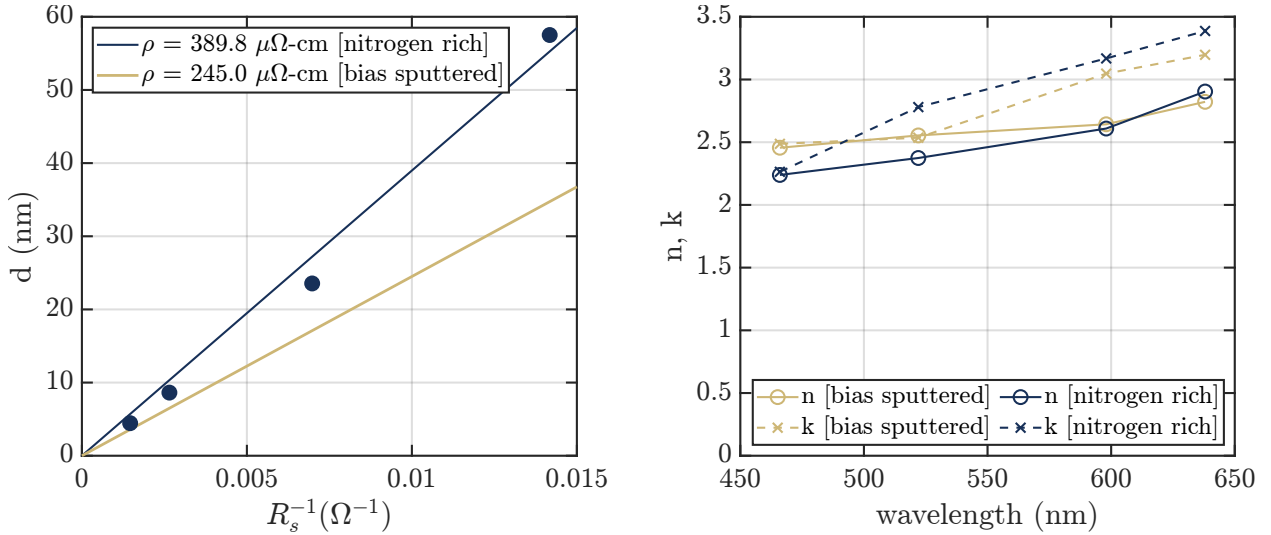


Figure 3-2: Left, thickness measurements of nitrogen rich NbN using a fixed angle ellipsometer. The solid blue line is a linear fit to the measured thickness where the slope is the resistivity,  $\rho$ . The yellow line is the resistivity for bias sputtered NbN. Right, optical constants determined from multi-sample ellipsometer measurements [63]. At longer wavelengths, we see that the absorption coefficient  $k$  is greater for nitrogen rich NbN.

wavelengths we see an increase in absorbance ( $k$ ) for the nitrogen rich NbN.

This section has demonstrated how adjusting the sputtering parameters change the electrical and superconducting properties. In general, this study showed that the  $RRM$  can be increased by increasing the Ar or  $N_2$  flow rates or by decreasing the temperature or thickness. However, these measurements do not reveal how the atomic structure of our thin film is changing.

### 3.3 Atomic structure characterization

Niobium nitride is a widely used material in superconducting devices [65, 66] thanks to its hardness [67], radiation tolerance [68], and high critical temperature [64]. However, the relation between the superconducting properties and the atomic structure is not well understood and is an active area of research in material science [69–71]. In this section we analyze the atomic structure of the bias sputtered and nitrogen rich NbN films to investigate the relation between photon detection and atomic structure.

The phase diagram of NbN has a wide range of compositions that form under different atomic weights and temperatures [72]. Pure niobium forms a face-centered cubic structure and the ideal

1:1 concentration of NbN forms a stable rocksalt structure. However, variations ( $\approx 10\%$ ) in the atomic concentrations can occur without affecting the crystal structure, making it difficult to identify the ideal stoichiometry. A work by Kalal et al. studied the atomic structure of NbN as nitrogen is introduced into the lattice through reactive sputtering [70]. They identified three regions that form: Nb with interstitial N, rocksalt NbN, and rocksalt NbN with interstitial N. As we transition between each phase, the critical temperature of NbN is known to form a dome shape for increasing nitrogen content [58, 59]. The reason for this roll off at high N concentrations is typically attributed to atomic disorder<sup>2</sup>.

Last year, the same authors who studied the evolution of NbN phases with N, attributed the reduction in critical temperature to interstitial N defects and Nb vacancies [69]. They were able to predict critical temperatures from the simulated density of states around the Fermi level which was spread due to the introduced defects. This was determined through x-ray absorption spectroscopy and *ab initio* simulations. Additionally, the interface between the film and substrate can influence the  $T_c$  [64]. The effect disorder has on  $T_c$  will consequently have an effect on the detection efficiency of SNSPDs. For this reason, it is important to understand the atomic structure of our material.

### 3.3.1 X-Ray diffraction

The analysis of NbN by XRD was performed in the Center of Material Science and Engineering department at MIT. We performed a grazing incidence ( $\angle 1^\circ$ ) x-ray diffraction using a Rigaku SmartLab which emits x-ray photons of wavelength  $\lambda \approx 1.54 \text{ \AA}$ . The XRD optics were configured with parallel beam, parallel slit analyzer, and a 5 mm incident length filter. After performing optics and sample alignments we performed a  $2\theta$  scan from  $10^\circ$  to  $80^\circ$  with steps of  $0.01^\circ$  while keeping the incident beam fixed. Performing this measurements lets us sample in-plane information of our sample. We deposited thick films (50 nm) of each composition on 300 nm  $\text{SiO}_2$  thermal oxide on silicon, ensuring there is sufficient material for x-ray analysis. The result of each measurement is shown in Figure 3-3. In Figure 3-3, XRD measurements for each composition are vertically shifted by an arbitrary amount. We find the nitrogen rich NbN has sharper and more defined peaks than the bias sputtered NbN. The peak width is inversely related to the

---

<sup>2</sup>see Ref. [59] supplemental material.

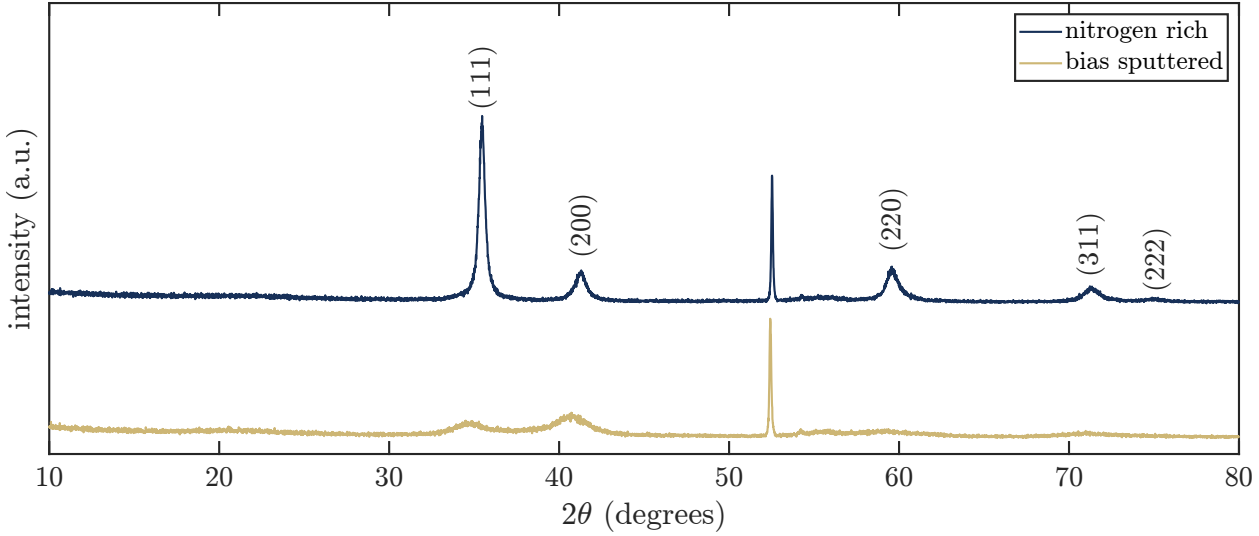


Figure 3-3: Grazing incidence x-ray diffraction measurement of two NbN compositions. These results show an increase in the crystalline phases for the nitrogen rich NbN. The peak at 52° corresponds to the substrate. The blue curve was offset by an arbitrary amount for clarity.

average crystallite size through the Scherrer equation (Eq. 3.1), where  $D$  is the average crystallite size,  $K$  is assumed unity,  $\beta$  is the width of each peak, and  $\theta$  is the Bragg angle. Using the (111) and (200) peaks, we calculate an average crystallite size of 4 nm for bias sputtered NbN and 14 nm for nitrogen rich.

$$D = \frac{K\lambda}{\beta \cos \theta} \quad (3.1)$$

We then index the peak angles with the crystallographic planes of cubic NbN and find an average lattice parameter of 4.42 Å for bias sputtered and 4.38 Å for nitrogen rich. The larger grain size is expected, however the lattice parameter is expected to increase as nitrogen is introduced. Overall, the nitrogen rich NbN agrees well with the  $\delta$ -NbN structure [70].

### 3.3.2 Transmission electron microscopy

TEM is one of the few tools at our disposal that can allow us to directly image the atomic structure of solids. Furthermore, selected area diffraction of a specimen can tell us about the overall texture or crystallinity of the material. We performed high resolution transmission electron microscopy and selected area diffraction using a JEOL 2010F TEM. Each film composition was sputtered onto a 5 nm thick silicon nitride TEM grid. While sputtering directly onto the TEM grid, reference samples were included in the deposition chamber to be used for film characterization. The refer-

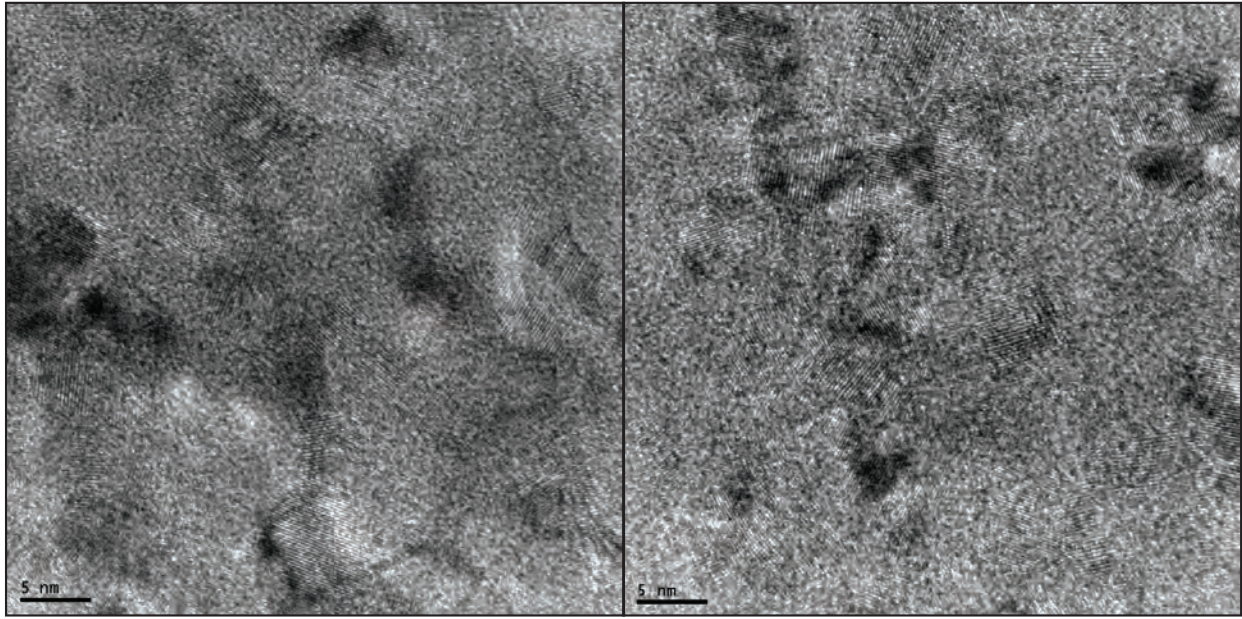


Figure 3-4: High resolution top-down transmission electron micrographs. Left, bias sputtered NbN. Right, nitrogen rich NbN. Qualitatively, the bias sputtered NbN appears to be less crystalline than the nitrogen rich NbN, as there are fewer regions of visible lattice order. The scale bar is equal to 5 nm.

ence samples had a thickness of  $20.5 \pm 1$  nm and critical temperatures of 9.25 K and 10.9 K for the bias sputtered and nitrogen rich respectively.

Figure 3-4 shows high resolution TEM images of each polycrystalline NbN film. In the left image, the bias sputtered NbN film has a qualitatively smoother appearance, as there are fewer regions with clearly visible crystalline ordering, when compared to the nitrogen rich film on the right. This aligns with our conclusion from the FWHM estimation of crystallite size using the XRD spectrum of each film. Beyond imaging the crystalline regions directly, we performed selected area electron diffraction for each polycrystalline film and show the annular diffraction patterns in Figure 3-5. The most notable difference between these two images is the clarity in which one is able to resolve the two concentric circles having an approximate radius of  $5\text{ nm}^{-1}$ . In the left figure, the smaller of the two circles is less visible than in the right image. Additionally, we see a slight dependence in the intensity of each ring on the radial angle. This variation along the circumference of the rings indicates the bias sputtered NbN has additional nonidealities (i.e. film texture) that are not present in the nitrogen rich film on average.

Figure 3-6 shows the center profile of the diffraction patterns in Figure 3-5. We find good

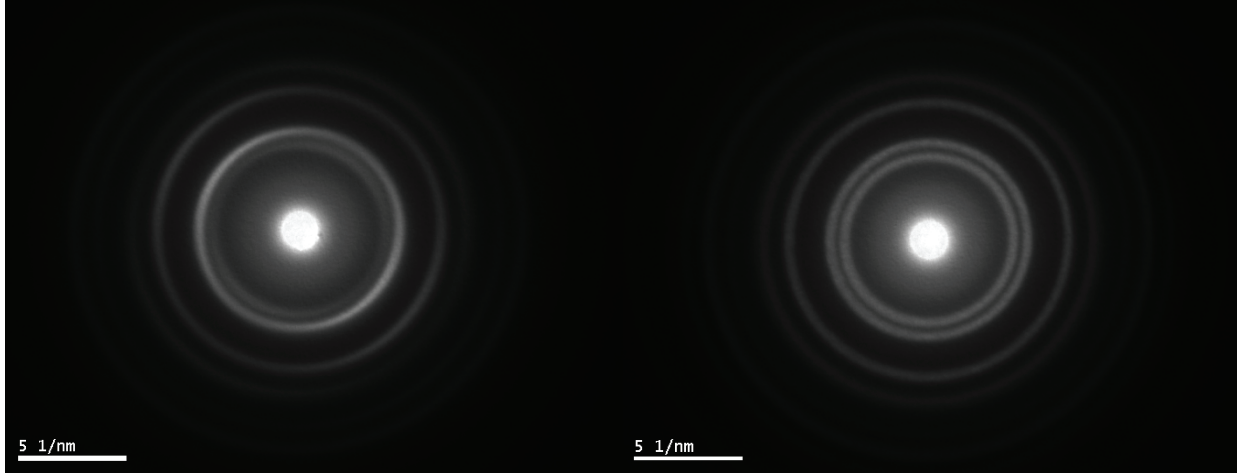


Figure 3-5: Selected area diffraction. Left, bias sputtered NbN. Right, nitrogen rich NbN. This measurement allows us to look at our material’s reciprocal lattice. Here we see annular diffraction patterns that indicate the polycrystalline nature of our films. Additionally, we note greater definition in the two brightest rings for the nitrogen rich NbN and a rotational variation for the bias sputtered NbN.

agreement with published diffraction patterns for NbN [73], and can determine the lattice parameter for comparison with the XRD results [74]. The lattice parameters were calculated to be  $4.40 \text{ \AA}$  for the bias sputtered NbN and  $4.43 \text{ \AA}$  for nitrogen rich NbN. These values are similar to the XRD analysis, but now we see the expected increase in the lattice parameter due to interstitial nitrogen.

In this chapter we have compared two compositions of NbN for micrometer wide SNSPDs and studied changes in the stoichiometry due to varying sputtering parameters. This analysis has shown that the nitrogen rich NbN—which was used to produce the first micrometer wide SNSPD [26]—has increased grain size compared to the bias sputtered NbN typically used in the our group. From the work by Kalal [70], the maximum  $T_c$  was achieved at a lattice parameter  $LP \approx 4.38 \text{ \AA}$  and a significant reduction in  $T_c$  was observed as the  $LP$  deviated from the optimal value. We find a similar relation with our films, assuming the XRD analysis to be accurate. This result conflicts with the general understanding that a lower  $T_c$  corresponds to a smaller gap  $\Delta$  and thus greater photon detection efficiency. As we will show in Chapter 4, the nitrogen rich NbN has greater detection efficiency than the bias sputtered NbN despite having generally higher  $T_c$ . This indicates that the atomic structure of our film plays an equally important role in determining not only the superconducting gap, but the other criteria for wide wire detection. For example, larger

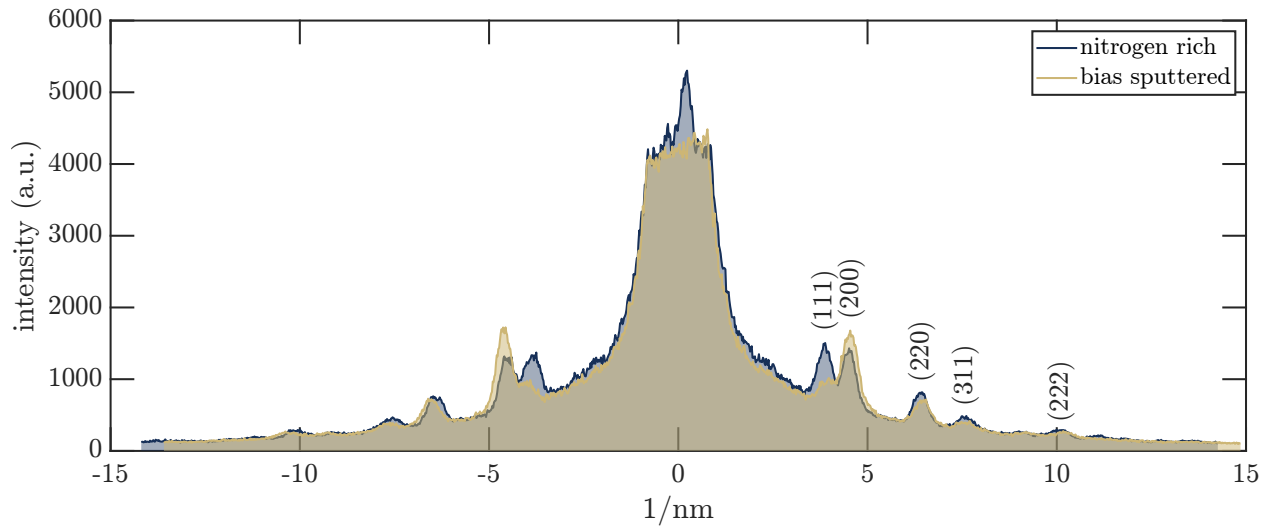


Figure 3-6: Center profile of the selected area diffraction patterns. The blue curve has two distinct peaks at the (111) and (200) planes, while the yellow curve has a single peak at (200). Lattice planes were identified in Ref. [73].

gain size reduces the total number of grain boundaries within a wire—boundaries that have the potential to suppress the critical current of a detector, thus lowering  $I_b/I_{dep}$ . We continue this discussion in the next chapter with greater attention on the performance of micrometer wide SNSPDs.



# Chapter 4

## Micrometer Wide Single Photon Detectors

Depending on the desired application, superconducting nanowire single photon detectors (SNSPDs) can be designed to maximize certain characteristics [75, 76]. Individual detectors have demonstrated ultra low jitter [77], mid-infrared sensitivity [78], near unity efficiency at telecommunication wavelengths [79], and low dark count rates (<1 per day) [22]. In order to achieve record breaking performance for each metric, the detector material and geometry is optimized in a way that inevitably reduces performance in the other metrics. In this chapter we will focus on improving the detection efficiency in micrometer wide single photon detectors.

Prior to the development of the kinetic-equation approach [25], the detection efficiency of a micrometer wide SNSPD at 1550 nm was assumed to be zero<sup>1</sup>. Since that time, a number of high efficiency micrometer wide SNSPDs have been reported; a collection of them are detailed in Table 1.1. Of these publications, the largest area detectors are made from amorphous silicides like WSi or MoSi. Unfortunately, these materials have low critical temperatures  $T_c < 4.2$  K that require operation in  $\leq 1$  K cryostats. Requiring high performance cryostats runs counter to the appeal of micrometer wide detectors, which remove the need for costly electron beam lithography, thus a higher  $T_c$  material is desired. Polycrystalline thin films of NbN or NbTiN [80] with  $T_c \sim 7\text{-}12$  K are suitable candidates. However, detectors made from these materials are more likely to have suppressed  $I_c$  due to constrictions, thus preventing large area detectors. For these reasons we

---

<sup>1</sup>For that energy photon, it was assumed that the hot spot diameter would be much smaller than the wire width.

have chosen to focus on low active area NbN detectors greater than  $1\text{ }\mu\text{m}$  wide.

## 4.1 Design and fabrication of wide detectors

In this section we discuss the design and fabrication of micrometer wide single photon detectors (SNSPDs). The design of micrometer wide SNSPDs varies slightly from nanometer wide detectors as the relative fraction of the depairing current becomes more significant. Details relating to the fabrication of the detectors follows the same process as presented in Section 2.2.1, however additional details specific to wide detectors will be presented here.

### 4.1.1 Design

For SNSPDs the term detection efficiency can mean different things. The system detection efficiency calculates (SDE) the ratio between photons sent to the detector and the number of counts recorded on the instrument. The internal detection efficiency (IDE) is the ratio between the number of absorbed photons and the number of counts recorded on the instrument. Generally speaking, IDE increases as a function of bias current. If the count rate no longer increases with current, then it is inferred that every absorbed photon produces a measurable count on the instrument. This appears as a plateau, or saturated region, in a photon count rate versus bias current curve (PCR curve), where an increase in bias current does not increase the count rate. A saturated detector is required for most practical applications due to the incurred loss from other parts of the system (i.e. coupling, absorption).

When describing the detection efficiency one must also specify the energy of the incident photon (or particle) on the detector. A detector with near unity efficiency at one wavelength will certainly have unity efficiency at a much shorter wavelength. For the majority of SNSPD demonstrations the target wavelength is 1550 nm; as it is the most commonly used wavelength in optical communication due to the low absorption in optical fibers.

The response of a detector biased at  $I_b \approx I_c$ , can exhibit one of two behaviors depending on the reset time. If the reset time  $\tau_r = L_k/R_L$  is too slow then the device will oscillate at high bias currents [81]. If the reset time is too fast then the device will latch; a term used to describe the detectors inability to self reset [82]. To avoid latching, the reset time can be increased either by

increasing the inductance or reducing the load resistance. For example, the nitrogen rich film has a sheet inductance of  $L_k \approx 1.378 R_s / T_c = 200 \text{ pH} / \square$ . For a device with 1000 squares a  $50 \Omega$  load resistance would result in  $\tau_r = 4 \text{ ns}$ ; for a  $10 \Omega$  load we have  $\tau_r = 20 \text{ ns}$ . For all devices the value of the shunt resistor was chosen such that  $\tau_r \approx 10\text{-}100 \text{ ns}$ .

The detector's reset time will effect the maximum count rate as well as the shape of the PCR curve. In a latching detector, the photon count rate will increase with bias current until either a sharp decrease (to zero) or a slight roll off. The roll off can be attributed to the device latching during the integration time. As the bias increases the device latches earlier in the integration window, thus recording fewer counts. In an oscillating detector, the PCR will begin to increase as the device begins to oscillate. This is the cumulative response of the oscillations and photon counts.

#### 4.1.2 Fabrication

Using the design principles of the previous section, meandered and straight wire SNSPDs with a wide range of inductances were designed. Each design was parameterized in Python and the optimal superconducting geometries [83] were generated using PHIDL [84]. The parameterized models are located in a GitHub repository that can be integrated with other Python packages like PHIDL or QNNPY (see Section 4.2).

The meander and straight detector designs are shown in the left and right of Figure 4-1, respectively. The meander is 200 nm wide with a pitch of 400 nm, resulting in a 33% fill factor over a  $100 \mu\text{m}^2$  area. The large meander in the right of Figure 4-1 is the series inductor while the  $3 \times 60 \mu\text{m}$  straight detector is folded above it. If the detector is to be read out in a single-ended readout, the unpatterned film can be used as ground, removing the need for a second bond pad. The size of the inductor was determined from the desired reset time and the inductor width was chosen to be  $3 \times$  greater than the detector width, to ensure no part of the inductor would produce counts. We can calculate the inductance of our device through the product of the sheet inductance and the number of squares  $\square = l/w$ . Due to the width of the inductor, the desired number of squares typically stretches over a  $500 \times 500 \mu\text{m}^2$  area. This area corresponds to the write area of a single field for our electron beam lithography tool. Any pattern that extends beyond this area must be written with multiple fields, introducing stitching errors between fields due to the lower

precision of the micromechanical sample stage. To avoid stitching errors, one could either use multipass—a procedure where the exposure dose is shared between fields, reducing the stitching error—or confine the desired pattern to within a single field, completely removing stitching error. In this work we opted for the latter option, and folded the straight detector horizontally within the top of the field. With the device design and fabrication complete we focus on the measurement and results in the next sections.

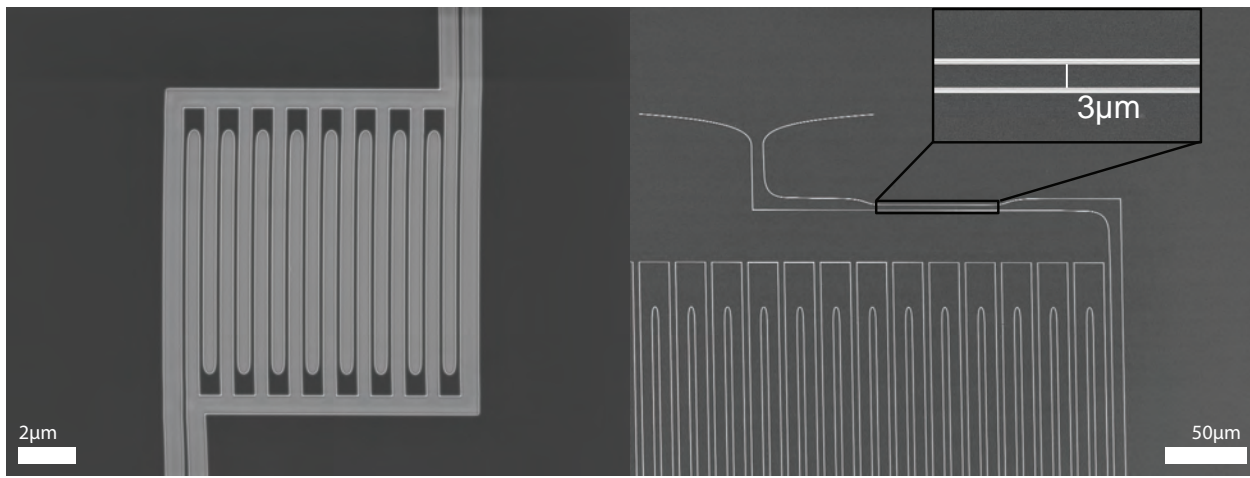


Figure 4-1: Scanning electron micrograph of two single photon detectors. The left image shows a 200 nm wide detector, meandered over  $10 \times 10 \mu\text{m}$  area. The dark regions are the NbN film and the light region is the substrate where the NbN has been etched away, similarly for the right figure. The right figure shows a  $3 \mu\text{m}$  wide detector in a straight configuration. The large meander below the detector is a series inductor to prevent latching.

## 4.2 Cryogenic measurement and data processing

In this section we discuss a typical measurement setup for micrometer wide single photon detectors. Despite having a greater signal to noise ratio than nanometer wide detectors, wide detectors requiring high critical currents can still be limited by noise from an improper setup. In this section we will discuss the cryogenic apparatus, the necessary instrumentation, and the methods for characterizing our detectors. Additionally, the final portion of this section will discuss an instrument control toolbox used to standardize our characterization.

### 4.2.1 Cryogenic setup

Since helium was first liquefied in 1911 by Kamerlingh Onnes [1], the field of low temperature physics and the development of cooling apparatus has continually matured. With the growth of quantum computing, commercial cryogenic systems readily achieve operating temperatures a few mK above absolute zero. The physics and engineering required to reach these temperatures represents some of the most sophisticated technology to date and is outside the scope of this thesis. However, we will briefly discuss the challenges associated with low temperature measurements as it pertains to the measurement of single photon detectors.

The central cooling component of a cryostat is referred to as the cold head. The cold head is designed to concentrate the maximum cooling power and lowest temperature to a single mechanical stage. The cryostat used in this work (ICE Oxford) has a large 1 K stage for sample mounting, shown in Figure 4-2. To mount a sample to the cold head we must ensure proper thermalization and provide the necessary electrical connections. To achieve this, we designed a custom printed circuit board (PCB) for sample mounting. The sample die is mounted to the PCB using GE thermal varnish in a region plated with electroless nickel immersion gold. The PCB is designed with many vias insuring low thermal resistance through either side of the PCB. The back of the PCB is free of any solder mask, leaving just gold, and coated in Apiezon thermal grease for greater thermal conduction when mounted to the 1 K stage. The PCB has a total of 8 sub-miniature push-on rf connectors for high-speed pulse readout from the detector. In addition, there are a total of 24 dc lines routed to  $2 \times 12$  Mill-Max multi-pin connectors for low-speed control and each dc line has a 0805 surface mount bias resistor in series. However, the bias resistors were instead used as shunt resistors by grounding each pin of the multi-pin connector to the PCB ground. The detector is illuminated via free space coupling from a fiber mount designed to fit the PCB footprint. Once installed in the cryostat, the room temperature resistance is measured from the cryostat's bulkhead connectors, thus ensuring proper electrical connection before cooling.

Figure 4-2 fully describes the technical details of the measurement. After mounting the sample it is enclosed by two thermal radiation shields and the outer vacuum canister. The cryostat is then put under a vacuum nominally equal to  $10^{-6}$  Torr using a turbomolecular pumping station prior to cooldown. The process of cooling down to near absolute zero is a dynamical one, due

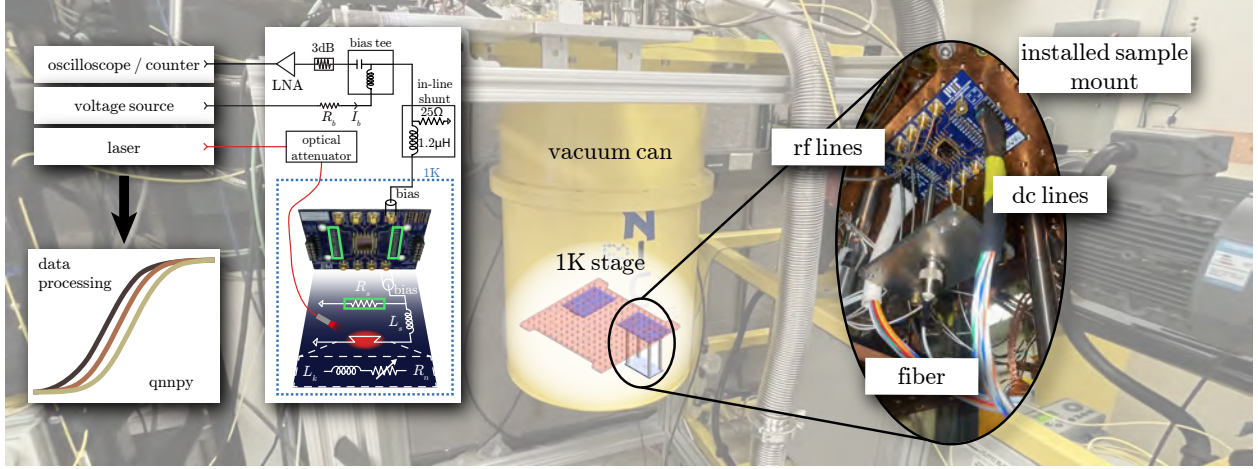


Figure 4-2: Cryogenic test setup for micrometer wide single photon detectors. The image background shows a snapshot of the closed-cycle cryostat. At the bottom of the yellow vacuum canister there is a rendering of the 1 K stage including the PCB and optical fiber stand. The right inset shows an image of the detector and the electrical and optical connections for a typical measurement. The left inset shows the room temperature measurement, typical measurement equipment, and a circuit diagram of the device under test.

environmental factors, or mechanical degradation of equipment. An algorithm for processing and visualizing the recorded data, which can be used to identify any performance degradation was developed. The total cooling procedure takes approximately 24 h, however the low base temperature and long term thermal stability is ideal for SNSPD measurement.

#### 4.2.2 SNSPD measurement

In this section we describe each measurement used to characterize our detector. The typical current-voltage (IV) behavior of a nanowire is shown in Figure 4-3(a). There are three regimes of interest in this IV curve: 1) superconducting, the vertical line at 0 V indicates zero resistance up to a critical value  $I_c$ ; 2) resistive, after the current exceeds  $I_c$  the voltage rapidly increases to a load line equivalent to the hot-spot resistance  $R_{hs}$ ; 3) retrapping, when decreasing the bias current the voltage follows the load line until less than the retrapping current  $I_r$ , where the nanowire returns to the superconducting state. After determining the  $I_c$  of the device it is biased to  $\approx 0.9I_c$  and the rf output is monitored on the oscilloscope with  $50\ \Omega$  coupling. At this point it is checked whether there are any visible dark counts. This tells us if we have a self-resetting detector or not. If the detector is unable to sustain dark counts, meaning it will register a few counts before

latching, it is unlikely to detect photons. In this case, the switching current is low<sup>2</sup> and the device is heavily constricted. The height of the pulse is proportional to the bias current times the hot spot resistance. It is also possible to resolve photon numbers from the pulse height [85]. After a detection event, positive and negative voltage pulses propagate out from the hot spot. Typically, we are able to observe the reflected negative pulse (Figure 4-3(b)) due to the impedance mismatch between our device and both ground and the  $50\Omega$  readout [66].

Having a large pulse relative to the noise floor allows for sharper thresholds when distinguishing between a photon count and the noise floor. When making this distinction, we connect the rf output of the SNSPD to a universal signal counter (Agilent 53131a). This specific counter injects noise into our system; it is recommended that a low pass filter (DC to  $\gg$ max count rate) be placed on the counter output. Bandwidth filtering is not ideal for collecting timing information, however for determining the count rate it has little effect. The counter is programmed to integrate the number of counts over a given period; where a count is defined as any positive crossing of a user defined threshold. Varying this threshold, or performing a trigger sweep, allows us to distinguish the arrival of a photon from no photon. Ideally this trigger sweep is performed at a set bias current and optical power point that results in a moderate count rate under illumination (light on) and few to zero dark counts with no illumination (light off). An example of such a plot is shown in Figure 4-3(c). The desired trigger value is one that is slightly above the noise floor, such counts from the lowest bias currents (i.e. lowest pulse heights) are not missed. A moderate threshold is shown in 4-3(b)

Keeping the trigger level and bias current at their respective values, the optical power can be varied. The power is controlled using an variable optical attenuator (JDS HA9), and we monitor the photon count rate. In the single photon counting regime, the count rate responds linearly with the attenuation with unity slope [86]. This indicates that we are producing a single count from the absorption of a single photon. If not in the linear regime it is inconclusive if a count resulted from a single photon or multi-photon process. This measurement should be repeated at the detector's highest efficiency. The linear function is shown in Figure 4-3(d).

As mentioned in 4.1, the detection efficiency of a SNSPD depends on the bias current ( $I_b$ ). To characterize a detector's IDE we ramp  $I_b$  and monitor the count rate. The count rate is determined

---

<sup>2</sup>Relative to the theoretical maximum (i.e. depairing) current  $I_{dep}$ .

by the counter's integration time, which can be increased if there is considerable noise present. This sweep is performed with the light off and the light on, which can be referred to as the dark count rate (DCR) and light count rate (LCR), respectively. The dark count rate is governed by electrical noise, black-body radiation, and intrinsic detector mechanisms, for increasing bias respectively [87]. We subtract the DCR from the light counts to produce the photon count rate (PCR). In an ideal PCR curve there would be a wide plateau where the onset of the flat portion of the plateau has zero dark counts. Examples of these curves are shown in Figure 4-3(e).

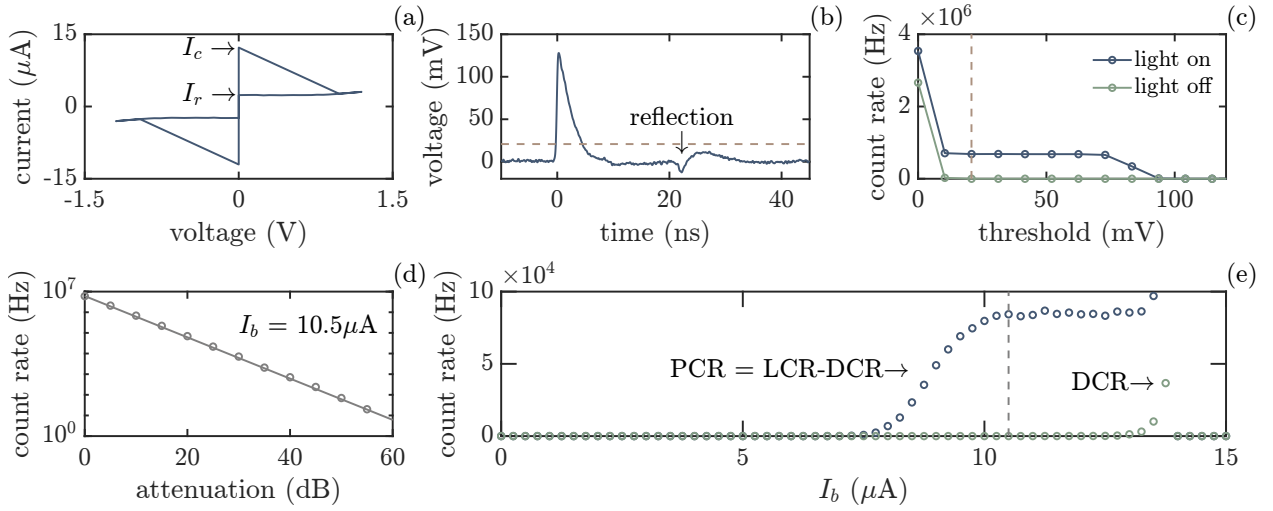


Figure 4-3: Overview of SNSPD characterization. (a) Current voltage characteristics of a nanowire; the critical current  $I_c$  and retrapping current  $I_r$ , is shown. (b) Output voltage pulse, the pulse threshold is shown as a dashed line. (c) The count rate as a function of threshold voltage. The lowest threshold samples the noise floor, the highest exceeds the pulse height. Any threshold in the flat region of ‘light on’ is acceptable. (d) Single-photon regime linearity check. (e) Count rate versus bias current curves. The dark count rate (DCR) is measured with the light off. The photon count rate (PCR) is the difference between the light count rate (LCR) and the DCR.

Collecting the measurement data, the external variables, and material and geometry information, builds a large and complex data set. To manage large data sets a number of proprietary or open source programs have been developed<sup>3</sup>. However, research often incorporates highly specific instruments with various remote programming formats, and connectivity. Existing solutions are often too rigid or too narrow in scope to fully address the needs of a dynamic research lab. Additionally, the ability of the lab to function becomes dependent on future versions and improvements of the external software. As a result, we internally developed QNNPY, a Python-

<sup>3</sup>For example, Keysight, National Instruments, Labber and QCodes have developed data acquisition frameworks.

based instrument control toolbox with easy to use, automated organizational infrastructure.

The structure of QNNPY is designed to separate the measurement *functions* from the measurement *settings*. Standardized and stand-alone functions lets us implement greater code management—like revision control—and establish best practices throughout the lab. Stand-alone settings allows us to ensure accurate record keeping, such as device characteristics, environmental factors, or applied signals. An example code block of QNNPY is shown in Listing 4.1.

---

```
import qnnpy.functions.snsdp as snsdp          # device-functions
config = r'Q:\somepath\configuration.yml'
#%%
c = snsdp.TriggerSweep(config)
c.run_sweep()
c.plot()
c.save()
```

---

Listing 4.1: Example code block for a measurement using the qnnpy package. Standardized measurement blocks parse user configuration files.

In the first two lines of Listing 4.1, we import the *functions* associated with the device under test, and define a configuration file which contains the *settings* for the measurement to be performed, respectively. The user then defines an object using the desired function (in this case *TriggerSweep*) which takes the configuration as an input. Each measurement is defined as a subclass within a device class (SNSPD) with functions that allows the user to record, visualize, and save data in a measurement-specific manner. Running the script shown in Listing 4.1 saves the data, plot, and settings in a remote directory automatically generated from the configuration file. Performing a measurement using QNNPY improves our data organization and reduces the risk of data loss through regularly timed backups.

Overall QNNPY improves our ability to easily record and manage data for SNSPD research. However, QNNPY does not cover the full range of measurements performed in the lab and currently limited to the measurements discussed. For novel measurement setups, the user can call the initial object definition to directly interact with connected instruments and use the base func-

tions for plotting and saving<sup>4</sup>. Additionally, it does not capture any information regarding the electrical circuit under test, which can cause a considerable difference between SNSPD measurements. We hope to address these problems in future versions. The code base can be found in a GitHub repository. Finally, all of the data originating from the QNN laboratory presented in this thesis was recorded using QNNPY.

## 4.3 Detector performance

In this section we characterize micrometer wide SNSPDs using the measurements described in the previous section. First, we will compare the intrinsic detection efficiency of nanometer wide detectors fabricated from the two NbN films described in Chapter 3. Second, increasingly wide detectors were fabricated using the nitrogen rich NbN. This section concludes with a discussion of the results and future work.

### 4.3.1 Material comparison

In this section we compare detectors fabricated from a nominal composition of NbN and one enriched with nitrogen. However, the process of making the film thinner is not discussed. Early attempts at fabricating wide detectors from ultra thin ( $<3\text{ nm}$ ) NbN in the lab were unsuccessful. We attribute this to the inhomogeneity of the sputtered polycrystalline film. However, suppression of the gap due to thickness could be performed using an epitaxial deposition method (e.g. atomic layer deposition [88]). To compare our materials, narrow detectors were fabricated from the films studied in Chapter 3 and are again referred to as "bias sputtered" and "nitrogen rich". Each detector (200 nm wide) was fabricated with identical geometry ( $10 \times 10\text{ }\mu\text{m}$  meander) and processing. We then performed the characterization described in Section 4.2 and find that the nitrogen rich sample reaches a higher fraction of the depairing current and has a longer plateau than the bias sputtered detector.

Figure 4-4 shows PCR curves for the two NbN compositions. For both film compositions, the onset of photon detection occurs at  $0.4I_{dep}$ . However, the maximum bias current reached is near  $0.8I_{dep}$  for the nitrogen rich sample and  $0.7I_{dep}$  for the bias sputtered sample. Additionally,

---

<sup>4</sup>This requires inputting some data manually; as humans, this will inevitably lead to errors.

sample	$R_s$ ( $\Omega/\square$ )	$d$ (nm)	$\rho$ ( $\mu\Omega\text{-cm}$ )	$T_c$ (K)	RRM	$L_k$ ( $\text{pH}/\square$ )	$I_c$ ( $\mu\text{A}$ )	$C$
bias sputtered	522	5.5	285.5	6.0	1.4	120	28.50	0.71
nitrogen rich	700	5.3	368.2	4.7	1.7	205	16.25	0.81

Table 4.1: Table of 200 nm wide SNSPD properties. Resistivity taken from fitting.

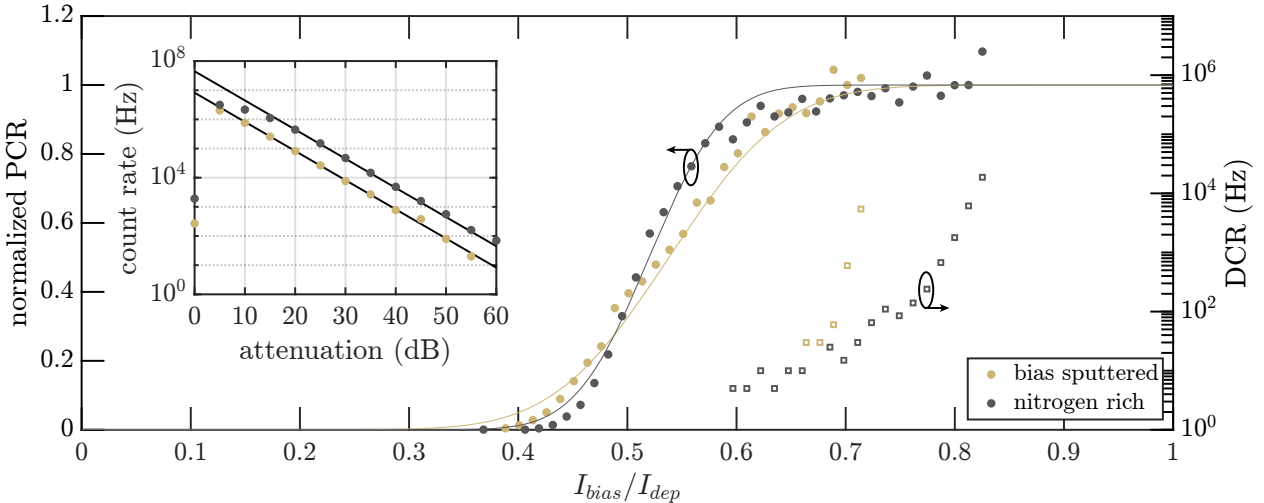


Figure 4-4: Count rate curves for 200 nm wide detectors. The left axis shows the normalized photon count rate; normalized to the last nonzero count rate. The nitrogen rich detector has a larger saturated region which reaches  $0.8I_{dep}$ . The solid lines are complementary error functions fit to the data [40]. The right axis shows the dark count rate in logarithmic scale. At  $I_c$ , the maximum DCR is lower for the nitrogen rich, indicating higher kinetic inductance. The inset shows the count rate as a function of optical attenuation. The fit line is linear with a slope of  $-1$ , where linearity implies the single photon regime.

the slope and maximum value of the intrinsic dark counts is reduced in the nitrogen rich film, indicating there are fewer material constrictions that produce counts without the arrival of a photon. The nitrogen rich detector meets the bias requirement ( $> 0.7I_{dep}$ ) for wide detectors, however, we will show in the following section that percentage of the depairing current achieved in wide wires is much lower.

### 4.3.2 Wide detector performance

In this section we evaluate the performance of wide NbN SNSPDs. The first investigation measures straight detectors with increasing widths and second measurement with increasing inductance. Through these experiments we observe saturated PCR curves in wires up to  $2.5\text{ }\mu\text{m}$  wide

and counts in the exponential regime for a  $3\text{ }\mu\text{m}$  wide detector. This showed that our material is nearly able to detect at  $3\text{ }\mu\text{m}$  wide and further reduction of the superconducting gap would allow us to move closer the plateau. To lower the gap, we fabricated new devices on a slightly thinner film ( $3.6\text{ nm}$ ). With the thinner film, we demonstrated saturated internal detection efficiency at  $1550\text{ nm}$  in a  $3\text{ }\mu\text{m}$  wide SNSPD. We conclude this section with a discussion of future work for the development of micrometer wide SNSPDs.

In the first experiment we measure devices with increasing width. The detector was designed as a straight detector with a large series inductance as described in Section 4.1.2. In addition to the series inductance, each detector was shunted with a low value surface mount resistor to ensure self-resetting. Each detector was then characterized using the methods described in Section 4.2.

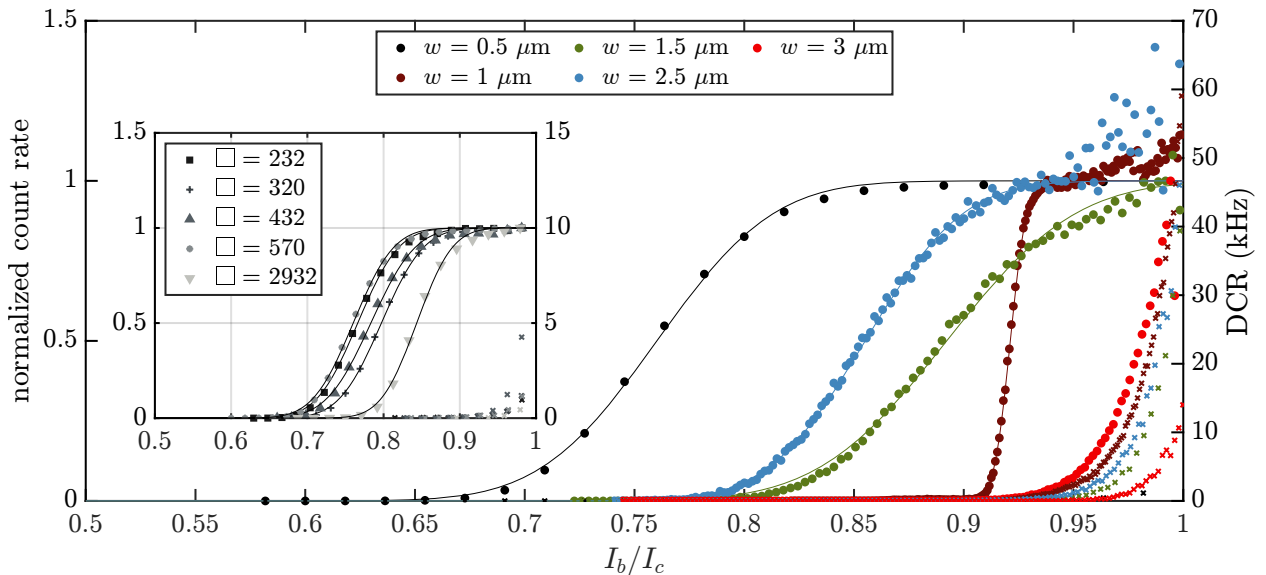


Figure 4-5: Photon count rate curves for detectors of different width under  $1550\text{ nm}$  illumination. The filled dots show the photon count rate normalized by the flattest region of the curve. If no plateau is present (i.e.  $1.5\text{ }\mu\text{m}$  &  $3\text{ }\mu\text{m}$ ) the counts were normalized by the maximum count rate. The solid lines are complementary error functions fit to the measured count rate. The right axis plots the dark count rate in kHz and is shown as crosses. The inset shows results of  $0.5\text{ }\mu\text{m}$  wide detectors with increasing series inductance. Each device was illuminated with the same optical power. The axis of the inset are in the same units as the main figure.

Figure 4-5 shows the photon count rate curves for five single photon detectors ranging from  $0.5\text{ }\mu\text{m}$  to  $3\text{ }\mu\text{m}$ . In this figure we can identify a few characteristics of our device. Most notable is the large plateau we see in the  $0.5\text{ }\mu\text{m}$  detector. The size of the plateau—or the region where we expect near unity internal detection efficiency—is expected to decrease as the width increases.

However, as the width increases we find nonuniform trends in the PCR curves. The detector with the next highest efficiency is the  $1.0\text{ }\mu\text{m}$  wide detector, followed by the  $2.5\text{ }\mu\text{m}$ ,  $1.5\text{ }\mu\text{m}$ , and  $3\text{ }\mu\text{m}$ . The nonuniformity in performance as width increases suggests that our devices are highly constricted. Another observable is the slope of the PCR curves is not dependent (or proportional) to the width. Specifically, the  $1\text{ }\mu\text{m}$  detector sees no counts until  $0.9I_c$  then the count rate sharply plateaus after a  $< 0.02I_c$  transition width. Additionally, the count rate for the  $1\text{ }\mu\text{m}$  and  $2.5\text{ }\mu\text{m}$  detectors is quite noisy at high bias currents. This is due to short integration times and relaxation oscillations that occur in shunted detectors.

The results of the second experiment is shown in the inset of Figure 4-5. A total of five  $0.5\text{ }\mu\text{m}$  wide and  $60\text{ }\mu\text{m}$  long detectors were fabricated with increasing series inductance. Each detector was characterized with the same optical power. If designed correctly, added inductance should have little effect on the efficiency of the of the detector; if all detection events occur in the detector, and not in the series inductor, we would expect the same IDE. We observe little to no dependence on the IDE as a function of inductance as evident by the PCR curves with equally broad plateaus.

Having produced wide detectors with saturated IDE, the jitter of each device was characterized. Jitter is the timing uncertainty between the input signal and the output signal. For example, in light detection and ranging (LIDAR) the distance from a source to an object is measured by the time of flight of the photons from the source, reflecting off an object, and being collected by a detector. The measured time between source and collection should be fixed for an object at a fixed distance. However, all detectors introduce some timing uncertainty (jitter) which is converted into uncertainty in the measured distance; zero jitter produces zero uncertainty in distance. The physical mechanism that causes jitter is an active area of research in SNSPDs physics [89–91]. In addition to the intrinsic jitter of the detection mechanism there is geometric jitter, a time delay caused by the spacial distribution of detection events within the detector area [66]. For the straight detectors studied here, the geometric jitter should be quite low due to the short length, while the intrinsic jitter in wide detectors will be much greater than traditional SNSPDs.

To measure the jitter of our devices we performed the following experiment. A  $10\text{ MHz}$  pulsed  $1550\text{ nm}$  laser was sent into a 50:50 optical splitter. One half of the splitter was sent into the cryostat, illuminating our SNSPD, while the other half was sent to a InGaAs based photodetector with a typical rise time of  $70\text{ ps}$ . The SNSPD output and the photodetector output were compared

on the oscilloscope using the maximum sample rate of 40 GS/s. Latency, or the delay between the two arrival times was subtracted and the arrival of each output pulse was time tagged at the fastest portion rising edge for each pulse. A total of 50,000 traces were recorded as a function of increasing bias current for each width. The results of this experiment are shown in Figure 4-6.

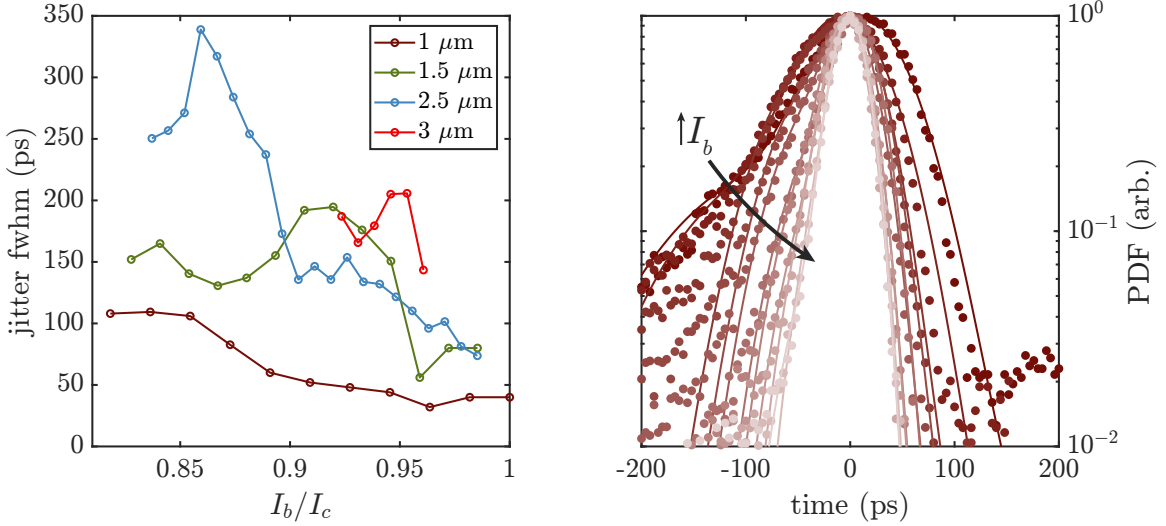


Figure 4-6: Device jitter as a function of bias current and width. The left figure shows the full width half maximum of the measured jitter. Matching colors with Figure 4-5 correspond to the same device. The right figure shows the probability density function of the measured time difference between the laser pulse and the photon arrival. Each bias point was fit with a two term Gaussian distribution. The full width half max of each of the curves in the right plot correspond to the 1  $\mu\text{m}$  trend in the left plot.

The left of Figure 4-6 shows the full width half maximum (FWHM) jitter as a function of bias current for the four widest widths. In general, we observe an increase in jitter as a function of width, which is likely a result of the increased distance a vortex must travel for photon absorption at the center verses the edge [46]. For the 1.5  $\mu\text{m}$  the jitter increases at  $0.9I_c$  forming a bump before decreasing to minimum values around  $0.95I_c$ . This is due to a shoulder that appears in the probability density function (PDF) at intermediate bias levels. The right of Figure 4-6 shows the PDF of the measured time between output pulses for the 1  $\mu\text{m}$  wide detector. The times were normalized around the center of the distribution, removing latency. The full width half max for each bias current was determined by fitting a Gaussian distribution to the measured data. In the right of Figure 4-6, there is the formation of a shoulder that decreases with increased bias. These shoulders are likely due to constricted regions in the wire having higher probability of

registering a count. This is the causal behavior for the dome behavior as bias is increased in the widest wires. Histograms of widths  $> 1 \mu\text{m}$  can be found in Appendix A.

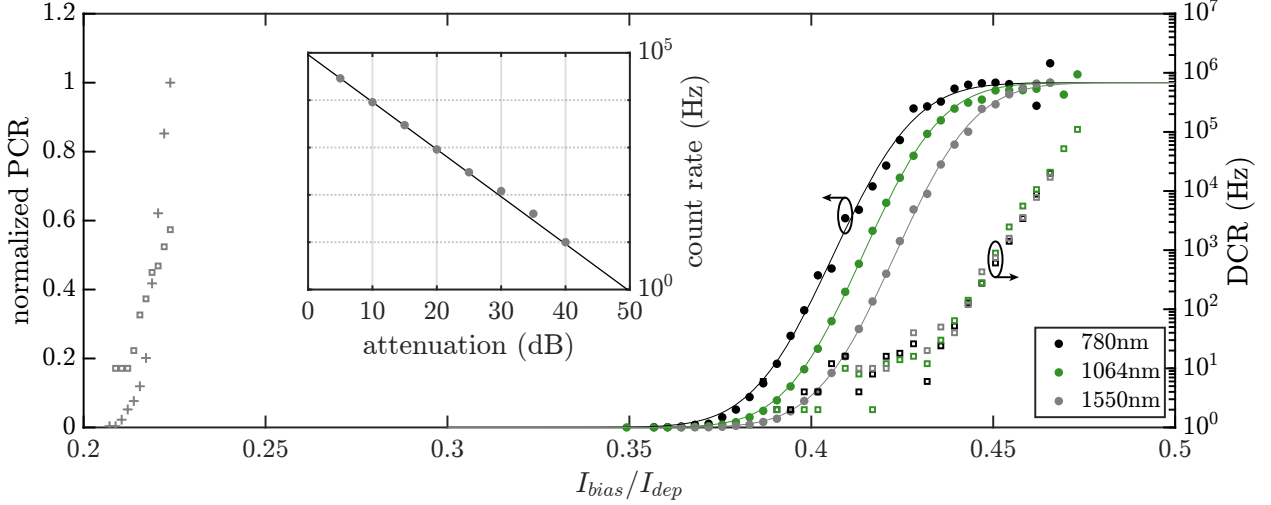


Figure 4-7: Photon count rate curves for  $3 \mu\text{m}$  wide detectors at various wavelengths. The normalized PCR as a function of the constriction factor  $C = I_{bias}/I_{dep}$  for the nitrogen rich film (dots) and the bias sputtered (crosses). Each curve of the nitrogen rich sample shows a saturated plateau. Dark counts for each measurement are plotted as squares. The inset shows the count rate as a function of attenuation for  $\lambda = 1550 \text{ nm}$  and  $I_{bias} = 0.43I_{dep}$ .

In the final experiment we further reduced the superconducting energy gap  $\Delta$  by decreasing the films thickness. We then follow the same design, fabrication, and measurement as previously detailed in this chapter. In Figure 4-7 we plot the normalized PCR curves for the  $3 \mu\text{m}$  detector at three wavelengths. The size of the plateau increases as the incident photon energy is increased. Although the DCR is independent of incident wavelength, it was measured each time and is plotted here to show the variation between measurements. In this plot the cross over from intrinsic dark counts to background infrared photons occurs around  $0.43I_{dep}$ . The maximum bias current of the nitrogen rich film  $0.47I_{dep}$ , less than the  $0.7I_{dep}$  needed for detection efficiency to be independent of the geometry [25]. However, the nitrogen rich detector is able to reach higher fractions of the depairing current than the bias sputtered detector.

### 4.3.3 Conclusion

This work discussed the performance of micrometer wide single photon detectors in two compositions of NbN. The widest detectors were fabricated from a composition that is closer to that

of  $\delta$ -NbN. This composition allowed for biasing at higher fractions of the depairing current and remained continuous at 3.6 nm thick. Wide NbN detectors are suitable candidates for the fabrication of large area SNSPD arrays. The high operating temperature, high signal to noise and large bias currents make them suitable for yielding large arrays using conventional foundry processes. The development of readout integrated circuits for SNSPD arrays and vertical integration of multiple detector planes would result in a high efficiency, high timing resolution, and low noise detector that could be used to capture rare events for dark matter search or particle trajectory reconstruction.

The relation between the atomic order of NbN and the detection efficiency was investigated in this work. Bias sputtered NbN detectors were heavily constricted, reaching just  $0.2I_{dep}$ . For nanowires, this constricted material might increase sensitivity, as the disorder increases local current density and therefore photon sensitivity at each constriction. For microwires, the nitrogen rich film with fewer constrictions yielded a  $3\text{ }\mu\text{m}$  wide SNSPD sensitive to 1550 nm photons. This result supports the requirement for wide detectors to be biased close to their depairing current, which is also evident from the superior performance of amorphous thin films. Large-area micrometer-wide NbN SNSPDs could be realized by fabricating epitaxial  $\delta$ -NbN films, thus minimizing constrictions while maintaining the advantages of NbN detectors. Finally, the measurement of critical current for wires exceeding the Pearl length showed a 30% increase in the depairing current as the temperature approached  $T_c$ . The physical mechanism for this is unclear, however, this increase could be leveraged for the development of even larger detectors where the detection area is localized to the regions of high current density formed by two dimensional screening and proximity effects.

## Appendix A

### Supporting information

One reason that the penetration depth would be much higher in Figure 2-5 is that the critical temperature is not constant from device to device. This effect, specific to changes in wire width was observed in MoSi samples ranging from 30 nm to 3  $\mu\text{m}$  [54].

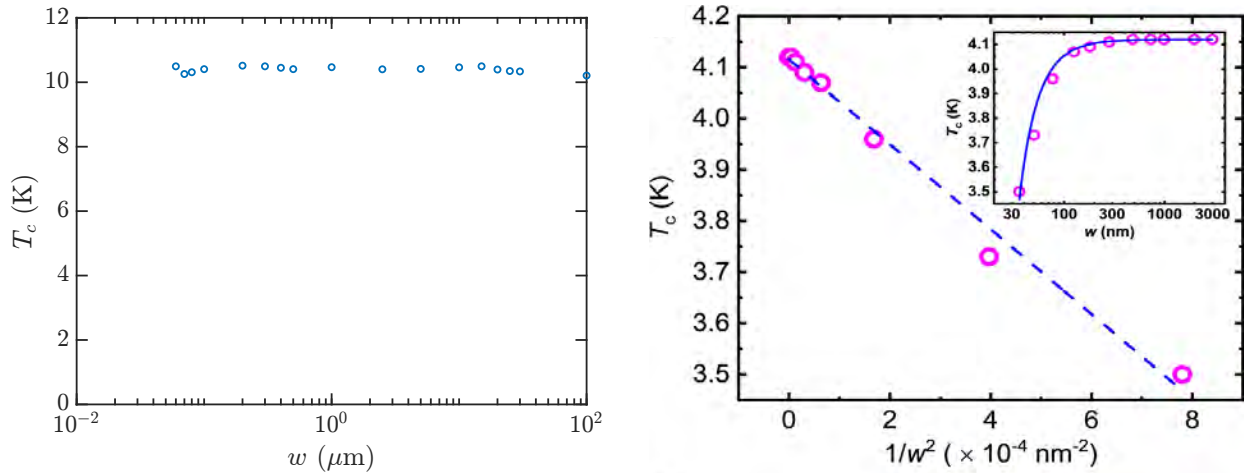


Figure A-1: Comparison of critical temperature measurements as a function of width. Left, NbN samples measured at MIT. Right, critical temperature measurements of MoSi wires as a function of width, reprinted from [54]

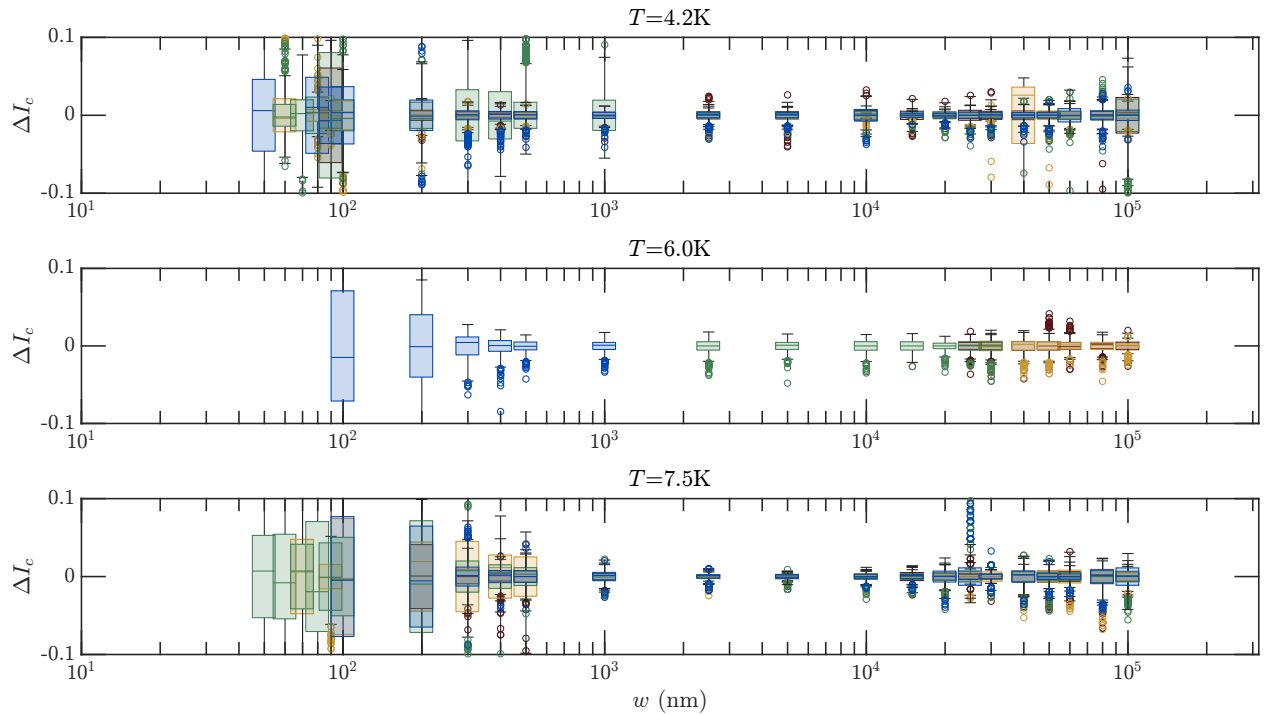


Figure A-2: Statistical data for the critical current measurements at three temperatures. Box plots of the critical current deviation from the mean. The edges of the box plot represent the first and third quartiles and the center line in the box plot represents the median. Outliers are defined as measurements greater than one and a half times the inter quartile range. Color indicates unique devices. Measurements are normalized by the mean. The majority of measurements vary less than 10% from the mean.

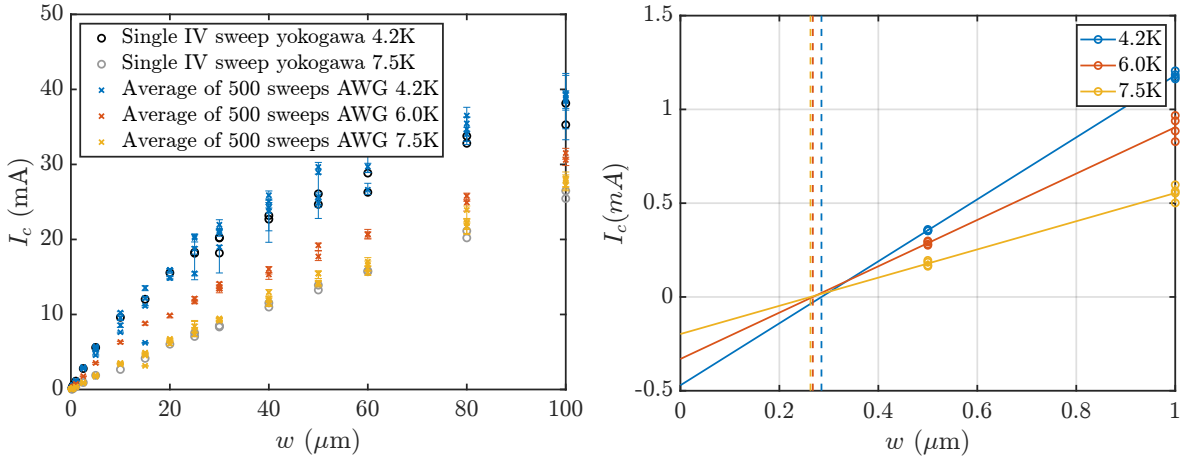


Figure A-3: Left, critical current measurements as a function of width. Distributions of critical current were performed at three temperatures and compared to baseline measurements using a Yokogawa GS200 current source. The critical current measured by the current source consistently returns a value lower than the distribution's mean. Each marker represents a unique device at a given temperature. Right, linear fitting to critical current measurements at three temperatures. As the temperature increases the intercept with zero critical current decreases; this indicates that the effective width of a wire is larger at higher temperature than at low temperature. A change in effective width supports the presence of a proximity effect.

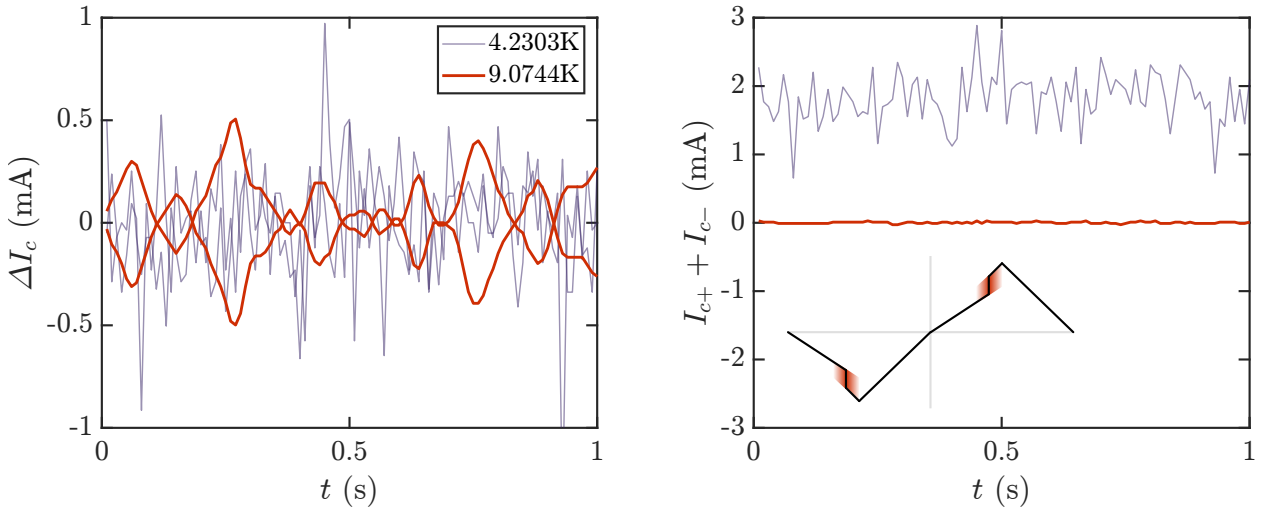


Figure A-4: Error in critical current measurements due to helium bubble formation. Left, two critical current measurements are plotted; one from the negative edge of the input ramp and one from the positive edge, for both temperatures. The low temperature data shows no correlation between positive and negative edges, while the high temperature data shows a periodic behavior. Right, the sum of the positive and negative critical currents is plotted for both temperatures. The low temperature data shows that the positive edge is typically higher than the negative edge. The high temperature data reveals the correlation between positive and negative measurements.

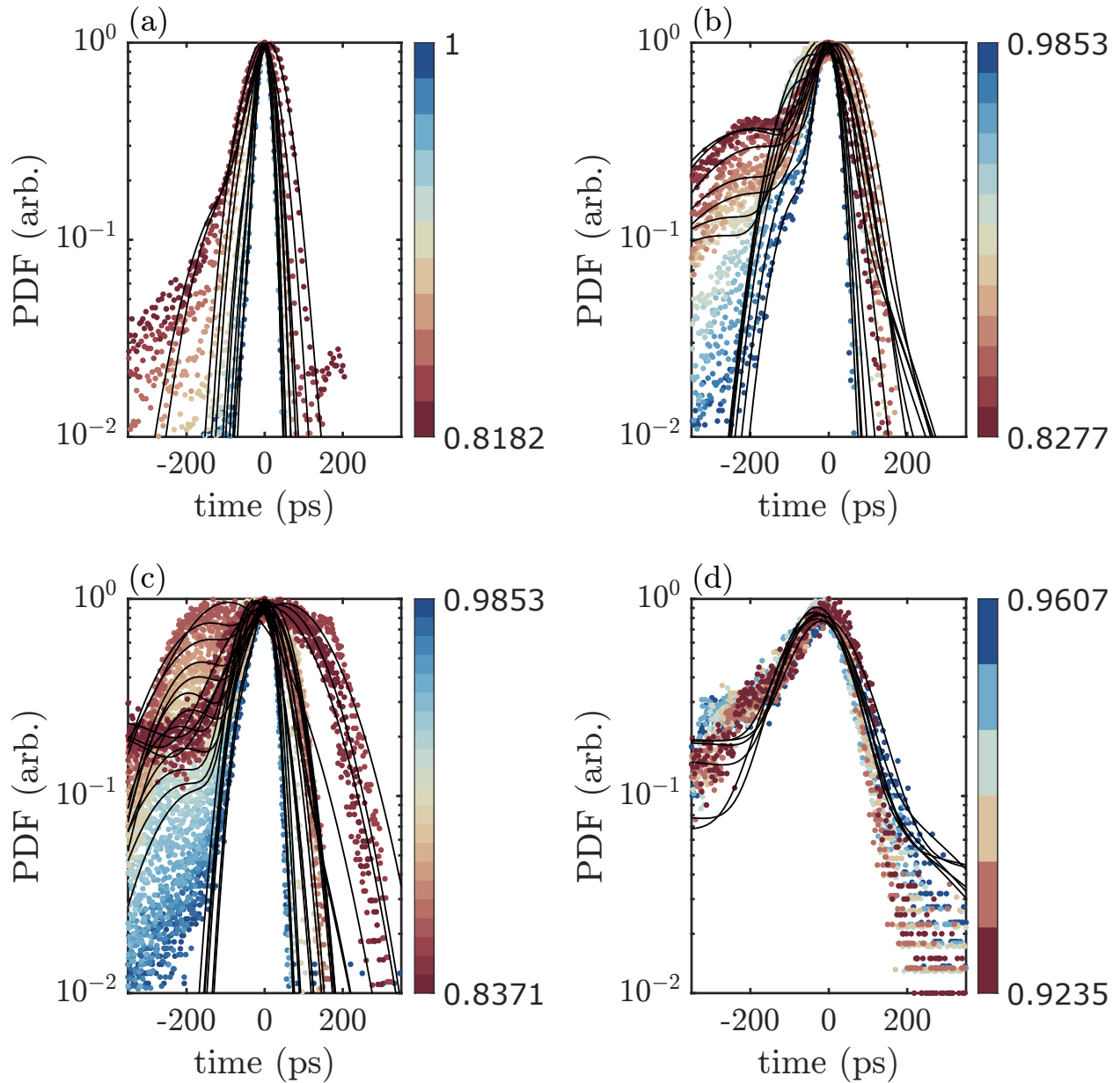


Figure A-5: Timing jitter between laser and SNSPD pulse for four detectors. (a)-(d) correspond to  $w = [1 \mu\text{m}, 1.5 \mu\text{m}, 2.5 \mu\text{m}, 3 \mu\text{m}]$  respectively. The color indicates the bias current relative to the critical current. The black lines are two term Gaussian distributions fit to the data.

# Bibliography

- [1] H Kamerlingh Onnes. research notebooks 56, 57. *Kamerlingh Onnes Archive, Boerhaave Museum, Leiden, the Netherlands*, 1911.
- [2] Walther Meissner and Robert Ochsenfeld. Ein neuer effekt bei eintritt der supraleitfähigkeit. *Naturwissenschaften*, 21(44):787–788, 1933.
- [3] J George Bednorz and K Alex Müller. Possible hight c superconductivity in the ba- la- cu- o system. *Zeitschrift für Physik B Condensed Matter*, 64(2):189–193, 1986.
- [4] Fritz London and Heinz London. The electromagnetic equations of the supraconductor. *Proceedings of the Royal Society of London. Series A-Mathematical and Physical Sciences*, 149(866):71–88, 1935.
- [5] John Bardeen, Leon N Cooper, and John Robert Schrieffer. Theory of superconductivity. *Physical review*, 108(5):1175, 1957.
- [6] Alexei Alexeyevich Abrikosov. The magnetic properties of superconducting alloys. *Journal of Physics and Chemistry of Solids*, 2(3):199–208, 1957.
- [7] Michael Tinkham. *Introduction to superconductivity*. Courier Corporation, 2004.
- [8] Terry P Orlando and Kevin A Delin. *Foundations of applied superconductivity*. Addison-Wesley, 1991.
- [9] Theodore Van Duzer and Charles William Turner. *Principles of superconductive devices and circuits*. 1981.
- [10] Alan M Kadin. *Introduction to superconducting circuits*. Wiley-Interscience, 1999.
- [11] F London. On the problem of the molecular theory of superconductivity. *Physical Review*, 74(5):562, 1948.
- [12] Armen Gulian. *Shortcut to superconductivity*. Springer, 2020.
- [13] Judea Pearl. *Vortex theory of superconductive memories*. PhD thesis, Polytechnic Institute of Brooklyn, 1965.
- [14] J Pearl. Current distribution in superconducting films carrying quantized fluxoids. *Applied Physics Letters*, 5(4):65–66, 1964.

- [15] Leon N Cooper. Bound electron pairs in a degenerate fermi gas. *Physical Review*, 104(4):1189, 1956.
- [16] RE Glover III and Ms Tinkham. Conductivity of superconducting films for photon energies between 0.3 and 40 ktc. *Physical Review*, 108(2):243, 1957.
- [17] Vitaly L Ginzburg and Lev D Landau. On the theory of superconductivity. In *On superconductivity and superfluidity*, pages 113–137. Springer, 2009.
- [18] AI Bezuglyj, VA Shklovskij, B Budinska, B Aichner, VM Bevz, M Yu Mikhailov, D Yu Vodolazov, W Lang, and OV Dobrovolskiy. Vortex jets generated by edge defects in current-carrying superconductor thin strips. *arXiv preprint arXiv:2204.06467*, 2022.
- [19] Saeed Khan, Bryce A Primavera, Jeff Chiles, Adam N McCaughan, Sonia M Buckley, Alexander N Tait, Adriana Lita, John Biesecker, Anna Fox, David Olaya, et al. Demonstration of superconducting optoelectronic single-photon synapses. *arXiv preprint arXiv:2204.09665*, 2022.
- [20] Alberto Boaron, Gianluca Boso, Davide Rusca, Cédric Vulliez, Claire Autebert, Misael Caloz, Matthieu Perrenoud, Gaëtan Gras, Félix Bussières, Ming-Jun Li, et al. Secure quantum key distribution over 421 km of optical fiber. *Physical review letters*, 121(19):190502, 2018.
- [21] Xingyu Zhang, Weijun Zhang, Hui Zhou, Xiaofu Zhang, Lixing You, Hao Li, Donghui Fan, Yiming Pan, Huiqin Yu, Lingyun Li, et al. NbN superconducting nanowire single-photon detector with 90.5% saturated system detection efficiency and 14.7 ps system jitter at 1550 nm wavelength. *IEEE Journal of Selected Topics in Quantum Electronics*, 28(5):1–8, 2022.
- [22] Yonit Hochberg, Ilya Charaev, Sae-Woo Nam, Varun Verma, Marco Colangelo, and Karl K Berggren. Detecting sub-geV dark matter with superconducting nanowires. *Physical review letters*, 123(15):151802, 2019.
- [23] Yonit Hochberg, Benjamin V Lehmann, Ilya Charaev, Jeff Chiles, Marco Colangelo, Sae Woo Nam, and Karl K Berggren. New constraints on dark matter from superconducting nanowires. *arXiv preprint arXiv:2110.01586*, 2021.
- [24] GN Gol’Tsman, O Okunev, G Chulkova, A Lipatov, A Semenov, K Smirnov, B Voronov, A Dzardanov, C Williams, and Roman Sobolewski. Picosecond superconducting single-photon optical detector. *Applied physics letters*, 79(6):705–707, 2001.
- [25] D Yu Vodolazov. Single-photon detection by a dirty current-carrying superconducting strip based on the kinetic-equation approach. *Physical Review Applied*, 7(3):034014, 2017.
- [26] Yu P Korneeva, D Yu Vodolazov, AV Semenov, IN Florya, N Simonov, E Baeva, AA Korneev, GN Goltsman, and TM Klapwijk. Optical single-photon detection in micrometer-scale nbn bridges. *Physical Review Applied*, 9(6):064037, 2018.
- [27] Jeff Chiles, Sonia M Buckley, Adriana Lita, Varun B Verma, Jason Allmaras, Boris Korzh, Matthew D Shaw, Jeffrey M Shainline, Richard P Mirin, and Sae Woo Nam. Superconducting microwire detectors based on wsi with single-photon sensitivity in the near-infrared. *Applied Physics Letters*, 116(24):242602, 2020.

- [28] Ilya Charaev, Yukimi Morimoto, Andrew Dane, Akshay Agarwal, Marco Colangelo, and Karl K Berggren. Large-area microwire mosi single-photon detectors at 1550 nm wavelength. *Applied Physics Letters*, 116(24):242603, 2020.
- [29] MD Shaw, Francesco Marsili, AD Beyer, JA Stern, GV Resta, Prasana Ravindran, S Chang, Joseph Bardin, DS Russell, JW Gin, et al. Arrays of wsi superconducting nanowire single photon detectors for deep-space optical communications. In *2015 Conference on Lasers and Electro-Optics (CLEO)*, pages 1–2. IEEE, 2015.
- [30] Jason Paul Allmaras. *Modeling and development of superconducting nanowire single-photon detectors*. PhD thesis, Caltech, 2020.
- [31] Alex D Semenov, Gregory N Gol'tsman, and Alexander A Korneev. Quantum detection by current carrying superconducting film. *Physica C: Superconductivity*, 351(4):349–356, 2001.
- [32] Alexei Semenov, Andreas Engel, H-W Hübers, Konstantin Il'in, and Michael Siegel. Spectral cut-off in the efficiency of the resistive state formation caused by absorption of a single-photon in current-carrying superconducting nano-strips. *The European Physical Journal B-Condensed Matter and Complex Systems*, 47(4):495–501, 2005.
- [33] D Yu Vodolazov. Current dependence of the red boundary of superconducting single-photon detectors in the modified hot-spot model. *Physical Review B*, 90(5):054515, 2014.
- [34] AG Kozorezov, Colin Lambert, Francesco Marsili, MJ Stevens, VB Verma, Jeffrey A Stern, Rob Horansky, Shellee Dyer, Shannon Duff, David P Pappas, et al. Quasiparticle recombination in hotspots in superconducting current-carrying nanowires. *Physical Review B*, 92(6):064504, 2015.
- [35] Koji Suzuki, Shigetomo Shiki, Masahiro Ukibe, Masaki Koike, Shigehito Miki, Zhen Wang, and Masataka Ohkubo. Hot-spot detection model in superconducting nano-stripline detector for kev ions. *Applied physics express*, 4(8):083101, 2011.
- [36] AN Zotova and D Yu Vodolazov. Intrinsic detection efficiency of superconducting nanowire single photon detector in the modified hot spot model. *Superconductor Science and Technology*, 27(12):125001, 2014.
- [37] R Lusche, A Semenov, K Ilin, M Siegel, Y Korneeva, A Trifonov, A Korneev, G Goltsman, Denis Vodolazov, and H-W Hübers. Effect of the wire width on the intrinsic detection efficiency of superconducting-nanowire single-photon detectors. *Journal of Applied Physics*, 116(4):043906, 2014.
- [38] AN Zotova and D Yu Vodolazov. Photon detection by current-carrying superconducting film: A time-dependent ginzburg-landau approach. *Physical Review B*, 85(2):024509, 2012.
- [39] D Yu Vodolazov, Yu P Korneeva, AV Semenov, AA Korneev, and GN Goltsman. Vortex-assisted mechanism of photon counting in a superconducting nanowire single-photon detector revealed by external magnetic field. *Physical Review B*, 92(10):104503, 2015.

- [40] AG Kozorezov, C Lambert, F Marsili, MJ Stevens, VB Verma, JP Allmaras, MD Shaw, RP Mirin, and Sae Woo Nam. Fano fluctuations in superconducting-nanowire single-photon detectors. *Physical Review B*, 96(5):054507, 2017.
- [41] John R Clem and VG Kogan. Kinetic impedance and depairing in thin and narrow superconducting films. *Physical Review B*, 86(17):174521, 2012.
- [42] M Yu Kupryanov and VF Lukichev. Temperature dependence of pair-breaking current in superconductors. *Sov. J. Low Temp. Phys.(Engl. Transl.);(United States)*, 6(4), 1980.
- [43] S Frasca, B Korzh, M Colangelo, D Zhu, AE Lita, JP Allmaras, EE Wollman, VB Verma, AE Dane, E Ramirez, et al. Determining the depairing current in superconducting nanowire single-photon detectors. *Physical Review B*, 100(5):054520, 2019.
- [44] Guang-Zhao Xu, Wei-Jun Zhang, Li-Xing You, Jia-Min Xiong, Xing-Qu Sun, Hao Huang, Xin Ou, Yi-Ming Pan, Chao-Lin Lv, Hao Li, et al. Superconducting microstrip single-photon detector with system detection efficiency over 90% at 1550 nm. *Photonics Research*, 9(6):958–967, 2021.
- [45] NN Manova, Eu O Smirnov, AA Korneev, GN Goltsman, et al. Superconducting photon counter for nanophotonics applications. In *Journal of Physics: Conference Series*, volume 1410, page 012147. IOP Publishing, 2019.
- [46] D Yu Vodolazov, NN Manova, Yu P Korneeva, and AA Korneev. Timing jitter in nbn superconducting microstrip single-photon detector. *Physical Review Applied*, 14(4):044041, 2020.
- [47] Dina Fazlizhanova. Inhomogeneous current distribution in superconductors. Master's thesis, Skolkovo Institute of Science and Technology, Moscow, Russia, 2020.
- [48] Joseph W Serene and Dierk Rainer. The quasiclassical approach to superfluid  $^3\text{He}$ . *Physics Reports*, 101(4):221–311, 1983.
- [49] Gert Eilenberger. Transformation of gorkov's equation for type ii superconductors into transport-like equations. *Zeitschrift für Physik A Hadrons and nuclei*, 214(2):195–213, 1968.
- [50] Wolfgang Belzig, Christoph Bruder, and Gerd Schön. Diamagnetic response of normal-metal–superconductor double layers. *Physical Review B*, 53(9):5727, 1996.
- [51] Klaus D Usadel. Generalized diffusion equation for superconducting alloys. *Physical Review Letters*, 25(8):507, 1970.
- [52] Adam Nykoruk McCaughan, Dylan M Oh, and Sae Woo Nam. A stochastic spice model for superconducting nanowire single photon detectors and other nanowire devices. *IEEE Transactions on Applied Superconductivity*, 29(5):1–4, 2019.
- [53] Ilya Charaev, T Silbernagel, B Bachowsky, Artem Kuzmin, Stefan Doerner, Konstantin Ilin, Alexej Semenov, D Roditchev, D Yu Vodolazov, and Michael Siegel. Proximity effect model of ultranarrow nbn strips. *Physical Review B*, 96(18):184517, 2017.

- [54] Qi Chen, Biao Zhang, La-bao Zhang, Fei-yan Li, Fei-fei Jin, Hang Han, Rui Ge, Guanglong He, Hao-chen Li, Jing-rou Tan, et al. Suppression of superconductivity dominated by proximity effect in amorphous mosi nanobelts. *Physical Review B*, 105(1):014516, 2022.
- [55] Brenden A Butters. *Digital and Microwave Superconducting Electronics and Experimental Apparatus*. PhD thesis, Massachusetts Institute of Technology, 2022.
- [56] Biao Zhang, Labao Zhang, Qi Chen, Yanqiu Guan, Guanglong He, Yue Fei, Xiaohan Wang, Jiayu Lyu, Jingrou Tan, Haochen Li, et al. Photon-assisted phase slips in superconducting nanowires. *Physical Review Applied*, 17(1):014032, 2022.
- [57] William D Sproul, David J Christie, and Dan C Carter. Control of reactive sputtering processes. *Thin solid films*, 491(1-2):1–17, 2005.
- [58] Tomas Polakovic, Sergi Lendinez, John E Pearson, Axel Hoffmann, Volodymyr Yefremenko, Clarence L Chang, Whitney Armstrong, Kawtar Hafidi, Goran Karapetrov, and Valentine Novosad. Room temperature deposition of superconducting niobium nitride films by ion beam assisted sputtering. *APL Materials*, 6(7):076107, 2018.
- [59] Andrew E Dane, Adam N McCaughan, Di Zhu, Qingyuan Zhao, Chung-Soo Kim, Niccolo Calandri, Akshay Agarwal, Francesco Bellei, and Karl K Berggren. Bias sputtered nbn and superconducting nanowire devices. *Applied Physics Letters*, 111(12):122601, 2017.
- [60] Benjamin Sacépé, Mikhail Feigel'man, and Teunis M Klapwijk. Quantum breakdown of superconductivity in low-dimensional materials. *Nature Physics*, 16(7):734–746, 2020.
- [61] Philipp I Zolotov, Alexander V Semenov, Alexander V Divochiy, Gregory N Goltzman, Nikita R Romanov, and Teunis M Klapwijk. Dependence of photon detection efficiency on normal-state sheet resistance in marginally superconducting films of nbn. *IEEE Transactions on Applied Superconductivity*, 31(5):1–5, 2021.
- [62] MV Burdastyh, SV Postolova, T Proslier, SS Ustavshikov, AV Antonov, VM Vinokur, and A Yu Mironov. Superconducting phase transitions in disordered nbtin films. *Scientific reports*, 10(1):1–7, 2020.
- [63] Owen Medeiros, Marco Colangelo, Ilya Charaev, and Karl K Berggren. Measuring thickness in thin nbn films for superconducting devices. *Journal of Vacuum Science & Technology A: Vacuum, Surfaces, and Films*, 37(4):041501, 2019.
- [64] Olivia G Licata, Jith Sarker, Mukesh Bachhav, Pinku Roy, Xiucheng Wei, Zihao Yang, Nag Patibandla, Hao Zeng, Mingwei Zhu, Quanxi Jia, et al. Correlation between thickness dependent nanoscale structural chemistry and superconducting properties of ultrathin epitaxial nbn films. *Materials Chemistry and Physics*, 282:125962, 2022.
- [65] Brenden A Butters, Reza Baghdadi, Murat Onen, Emily A Toomey, Owen Medeiros, and Karl K Berggren. A scalable superconducting nanowire memory cell and preliminary array test. *Superconductor Science and Technology*, 34(3):035003, 2021.

- [66] Marco Colangelo, Andrew Beyer, Boris Korzh, Jason P Allmaras, Andrew Mueller, Ryan M Briggs, Bruce Bumble, Marcus Runyan, Martin J Stevens, Adam McCaughan, et al. Impedance-matched differential snspsds for practical photon counting with sub-10 ps timing jitter. In *CLEO: QELS\_Fundamental Science*, pages FW2P–1. Optical Society of America, 2021.
- [67] M Benkahoul, E Martinez, A Karimi, R Sanjinés, and F Lévy. Structural and mechanical properties of sputtered cubic and hexagonal nbnx thin films. *Surface and Coatings Technology*, 180:178–183, 2004.
- [68] P Gregshammer, HW Weber, RT Kampwirth, and KE Gray. The effects of high-fluence neutron irradiation on the superconducting properties of magnetron sputtered nbn films. *Journal of applied physics*, 64(3):1301–1306, 1988.
- [69] Shailesh Kalal, Sanjay Nayak, Akhil Tayal, Jens Birch, Rajeev Rawat, and Mukul Gupta. Effect of disorder on superconductivity of nbn thin films studied using x-ray absorption spectroscopy. *Journal of Physics: Condensed Matter*, 33(30):305401, 2021.
- [70] Shailesh Kalal, Mukul Gupta, and Rajeev Rawat. N concentration effects on structure and superconductivity of nbn thin films. *Journal of Alloys and Compounds*, 851:155925, 2021.
- [71] Serhii Volkov, Maros Gregor, Tomas Roch, Leonid Satrapinskyy, Branislav Grančič, Tomas Fiantok, and Andrej Plecenik. Superconducting properties of very high quality nbn thin films grown by pulsed laser deposition. *Journal of Electrical Engineering*, 70(7):89–94, 2019.
- [72] Nurhan Cansever, M Danışman, and K Kazmanlı. The effect of nitrogen pressure on cathodic arc deposited nbn thin films. *Surface and Coatings Technology*, 202(24):5919–5923, 2008.
- [73] N Terao. New phases of niobium nitride. *Journal of the Less Common Metals*, 23(2):159–169, 1971.
- [74] CT Schamp and WA Jesser. On the measurement of lattice parameters in a collection of nanoparticles by transmission electron diffraction. *Ultramicroscopy*, 103(2):165–172, 2005.
- [75] Chandra M Natarajan, Michael G Tanner, and Robert H Hadfield. Superconducting nanowire single-photon detectors: physics and applications. *Superconductor science and technology*, 25(6):063001, 2012.
- [76] Alexej D Semenov. Superconducting nanostrip single-photon detectors some fundamental aspects in detection mechanism, technology and performance. *Superconductor Science and Technology*, 34(5):054002, 2021.
- [77] Boris Korzh, Qing-Yuan Zhao, Jason P Allmaras, Simone Frasca, Travis M Autry, Eric A Bersin, Andrew D Beyer, Ryan M Briggs, Bruce Bumble, Marco Colangelo, et al. Demonstration of sub-3 ps temporal resolution with a superconducting nanowire single-photon detector. *Nature Photonics*, 14(4):250–255, 2020.

- [78] VB Verma, B Korzh, AB Walter, AE Lita, RM Briggs, M Colangelo, Y Zhai, EE Wollman, AD Beyer, JP Allmaras, et al. Single-photon detection in the mid-infrared up to 10 micron wavelength using tungsten silicide superconducting nanowire detectors. *arXiv preprint arXiv:2012.09979*, 2020.
- [79] Dileep V Reddy, Robert R Nerem, Sae Woo Nam, Richard P Mirin, and Varun B Verma. Superconducting nanowire single-photon detectors with 98% system detection efficiency at 1550 nm. *Optica*, 7(12):1649–1653, 2020.
- [80] Stephan Steinhauer, Lily Yang, Samuel Gyger, Thomas Lettner, Carlos Errando-Herranz, Klaus D Jöns, Mohammad Amin Baghban, Katia Gallo, Julien Zichi, and Val Zwiller. Nbtin thin films for superconducting photon detectors on photonic and two-dimensional materials. *Applied Physics Letters*, 116(17):171101, 2020.
- [81] Emily Toomey, Qing-Yuan Zhao, Adam N McCaughan, and Karl K Berggren. Frequency pulling and mixing of relaxation oscillations in superconducting nanowires. *Physical Review Applied*, 9(6):064021, 2018.
- [82] Anthony J Annunziata, Orlando Quaranta, Daniel F Santavicca, Alessandro Casaburi, Luigi Frunzio, Mikkel Ejrnaes, Michael J Rooks, Roberto Cristiano, Sergio Pagano, Aviad Frydman, et al. Reset dynamics and latching in niobium superconducting nanowire single-photon detectors. *Journal of Applied Physics*, 108(8):084507, 2010.
- [83] John R Clem and Karl K Berggren. Geometry-dependent critical currents in superconducting nanocircuits. *Physical Review B*, 84(17):174510, 2011.
- [84] Adam N McCaughan, Alexander N Tait, Sonia M Buckley, Dylan M Oh, Jeffrey T Chiles, Jeffrey M Shainline, and Sae Woo Nam. Phidl: Python-based layout and geometry creation for nanolithography. *Journal of Vacuum Science & Technology B, Nanotechnology and Microelectronics: Materials, Processing, Measurement, and Phenomena*, 39(6):062601, 2021.
- [85] Sonia M Buckley, Alexander N Tait, Jeffrey Chiles, Adam N McCaughan, Saeed Khan, Richard P Mirin, Sae Woo Nam, and Jeffrey M Shainline. Integrated-photonic characterization of single-photon detectors for use in neuromorphic synapses. *Physical Review Applied*, 14(5):054008, 2020.
- [86] Marco Colangelo. Development of resistor process for the fabrication of shunted superconducting nanowire single photon detectors (snspd). Master’s thesis, Massachusetts Institute of Technology, 2017.
- [87] Oliver Kahl, Simone Ferrari, Vadim Kovalyuk, Gregory N Goltzman, Alexander Korneev, and Wolfram HP Pernice. Waveguide integrated superconducting single-photon detectors with high internal quantum efficiency at telecom wavelengths. *Scientific reports*, 5(1):1–11, 2015.
- [88] Risheng Cheng, Sihaio Wang, and Hong X Tang. Superconducting nanowire single-photon detectors fabricated from atomic-layer-deposited nbn. *Applied Physics Letters*, 115(24):241101, 2019.

- [89] D Yu Vodolazov. Minimal timing jitter in superconducting nanowire single-photon detectors. *Physical Review Applied*, 11(1):014016, 2019.
- [90] Mariia Sidorova, Alexej Semenov, Heinz-Wilhelm Hübers, Artem Kuzmin, Steffen Doerner, Konstantin Ilin, Michael Siegel, Ilya Charaev, and Denis Vodolazov. Timing jitter in photon detection by straight superconducting nanowires: Effect of magnetic field and photon flux. *Physical Review B*, 98(13):134504, 2018.
- [91] Jason P Allmaras, Alexander G Kozorezov, Boris A Korzh, Karl K Berggren, and Matthew D Shaw. Intrinsic timing jitter and latency in superconducting nanowire single-photon detectors. *Physical Review Applied*, 11(3):034062, 2019.